Contents lists available at ScienceDirect

Arabian Journal of Chemistry

journal homepage: www.ksu.edu.sa

Original article

Pharmacodynamic material basis and mechanism of Tenghuang Jiangu Wan on osteoarthritis using UPLC-Q-TOF-MS integrated with target network pharmacology

Dong Xie [a], Guangfu Lv [a], Yuchen Wang [a], Wenjing Zhang [a], Nian Li [a], Yao Duan [a], Qing Huang [b], Ge Chen [b], Zifeng Pi [a,*], Hao Yue [a,*]

[a] Jilin Ginseng Academy, College of Pharmacy, College of Management, Changchun University of Chinese Medicine, Changchun 130117, China
[b] Changchun People Pharmaceutical Group Co., LTD., Changchun 130033, China

ARTICLE INFO

Keywords:
Tenghuang Jiangu Wan
UPLC-Q-TOF-MS
Osteoarthritis
Pharmacodynamic material basis
Target network pharmacology
Mechanism

ABSTRACT

Tenghuang Jiangu Wan (THJGW) is a commonly utilized treatment for osteoarthritis (OA), yet its pharmacodynamic material basis and molecular mechanism remain inadequately understood. This study systematically characterized the in *vitro* and in *vivo* chemical components of THJGW using ultra-performance liquid chromatography-quadrupole time-of-flight mass spectrometry (UPLC-Q-TOF-MS). The pharmacodynamic material basis of THJGW in the treatment of OA was explored through a target network pharmacology approach and molecular docking technology. Cellular experiments were subsequently employed to validate the molecular mechanisms. Consequently, a total of 134 components from THJGW were identified in *vitro*, comprising 45 flavonoids, 10 iridoid glycosides, 39 phenylethanoid glycosides, 9 phenylpropanoids, 11 organic acids, 4 phenolics, and 16 other compounds. Additionally, 38 prototype absorbed components in serum were characterized for the purpose of network construction. 11 key components and 10 core targets (VEGFA, STAT3, RELA/NF-κB p65, PIK3R1, PIK3CA, MMP9, MMP1, IL-6, HDAC1, and FGF2) were determined by the target network pharmacology. Through Gene Ontology (GO) enrichment and Kyoto Encyclopedia of Genes and Genomes (KEGG) pathway analysis, it was found that these intersection targets are associated with various signaling pathways such as pathways in cancer, lipid and atherosclerosis, and prostate cancer. Notably, the lipid and atherosclerosis pathway was closely linked to OA. The molecular docking results demonstrated strong binding affinities of the three core targets: IL-6, STAT3, and RELA/NF-κB p65. These results suggest that these targets may play a significant role for THJGW in treating OA. In *vitro* experiments showed that THJGW had notable protective effects on LPS-induced RAW264.7 macrophages by reducing levels of TNF-α and IL-6, and inhibiting phosphorylation expression of STAT3 and NF-κB p65 proteins related to the lipid and atherosclerosis pathway. This study provides insight into the pharmacodynamic material basis and mechanism of action for THJGW in the treatment of OA, which provide scientific evidence for the scientific application and improvement of quality standards for THJGW.

1. Introduction

Osteoarthritis (OA) is a prevalent degenerative joint disease in clinical settings, characterized by cartilage degeneration, bone remodeling, osteophyte formation, joint inflammation, and loss of normal joint function. This leads to symptoms like joint pain, swelling, and limited movement, significantly impacting individuals' overall health and quality of life (Kraus et al., 2015). Currently, common drugs used to manage symptoms and restore joint function, such as non-steroidal anti-inflammatory drugs and glucocorticoids, not only harm the digestive tract, liver, and kidney function but also accelerate arthritis progression in the long term (Sharma, 2021). Current medical research reveals that traditional Chinese medicine (TCM) has shown great potential and advantages in the prevention and treatment of OA, owing to its abundant resources, good efficacy, and fewer side effects (Chen et al., 2023). Tenghuang Jiangu Wan (THJGW) is a TCM formula, derived from the

* Corresponding authors at: Changchun University of Chinese Medicine, No.1035, Boshuo Road, Jingyue National High-tech Industrial Development Zone, Changchun, China.
E-mail addresses: 178521212@qq.com, yuehao@ccucm.edu.cn (H. Yue).

https://doi.org/10.1016/j.arabjc.2024.105711
Received 3 October 2023; Accepted 3 March 2024
Available online 6 March 2024

extensive clinical experience of renowned Chinese medicine expert Professor Bailing Liu, which has shown good clinical efficacy in the treatment of OA. Its prescription has seven herbal medicines, including *Rehmannia glutinosa* (Gaertn.) Libosch ex Fisch. et Mey. (Radix Rehmanniae Praeparata), *Pyrola calliantha* H. Andres (Pyrola), *Epimedium brevicornu* Maxim. (Epimedium brevicornum), *Drynaria fortunei* (Kunze) J. Sm. (Rhizoma Drynariae), *Cistanche deserticola* Y. C. Ma. (Desertliving Cistanche), *Spatholobus suberectus* Dunn (Spatholobus), and *Raphanus sativus* L. (Radish Seed). Oral administration of the Tenghuang Jiangu (THJG) formula has been shown in studies to slow OA progression by inhibiting catabolic factor expression and subchondral bone sclerosis (Li et al., 2021). Furthermore, the THJG capsule has been shown to improve articular cartilage tissue injury in rats by decreasing the expression of inflammatory factors, resulting in fewer OA-related pain symptoms (Yan et al., 2020). However, more research is required to determine the pharmacodynamic material basis and mechanism of action for THJGW in treating OA.

Ultra-performance liquid chromatography-quadrupole time-of-flight mass spectrometry (UPLC-Q-TOF-MS) is an analytical tool with high resolution, high sensitivity, and structural characterization capabilities that has been widely used to analyze chemical components analysis in TCM (Kang et al., 2012). Network pharmacology converts the "one-target, one-drug" model into a "multi-components, multi-targets" model and has emerged as a powerful tool for investigating complex diseases and revealing the complex relationships between proteins, diseases, and drugs (Cheng et al., 2018). Traditional network pharmacology usually combines with pharmacokinetic parameters to predict absorption in *vivo* and mechanisms of drugs. Lin et al. analyzed the pharmacokinetic features of 16 absorbed components in rat plasma after oral administration of Wendan decoction at three different dosages, and subsequently, a total of 10 core components and targets were screened out through network pharmacology (Lin et al., 2023). Liu et al. explored the mechanism of pharmacokinetic target components of San-Ye-Tang-Zhi-Qing formula in the treatment of type 2 diabetes mellitus on the basis of network pharmacology, which indicated five analytes were absorbed and eliminated quickly in vivo, and explained their pharmacological mechanisms (Liu et al., 2020). Another study demonstrated a network pharmacology-integrated pharmacokinetics strategy to explore the pharmacological mechanisms of the major nine ingredients of Xianglian pill in ulcerative colitis treatment (Liu et al., 2021). However, the traditional network pharmacology process is cumbersome and the results may not be accurate. Target network pharmacology uses absorbed components in blood as candidates and integrates network pharmacology methods to investigate the mechanism of action for Chinese medicine, potentially reducing the number of false positive target sites discovered by traditional network pharmacology (Xu et al., 2017). Molecular docking is primarily used to investigate the intermolecular binding manner and interaction relationship, allowing prediction for the docking pattern and binding affinity of drug ligands and protein receptors, which is one of the most important methods to ensuring the reliability of network pharmacology predictions (Wang et al., 2021).

In this study, firstly, the in *vitro* and in *vivo* chemical components of THJGW were systematically analyzed and characterized by using UPLC-Q-TOF-MS technology combined with UNIFI software to shed light on its in *vitro* and in *vivo* chemical profile. Secondly, using target network pharmacology and molecular docking, potential active ingredients, targets, and mechanisms of action in the treatment of OA with THJGW were identified. Finally, experimental validation was performed on the predicted key targets, revealing the pharmacodynamic material basis and mechanism of action of THJGW in the treatment of OA.

2. Materials and methods

2.1. Chemicals and reagents

THJGW was provided by Changchun People Pharmaceutical Group Co., Ltd. (Changchun, China). Reference standards for icariin, icariside II, naringin, acteoside, echinacoside, D-(-)-quinic acid, and geniposidic acid were obtained from Shanghai Yuanye Bio-Technology Co., Ltd. (Shanghai, China). The purity of the aforementioned standards exceeded 98 % (HPLC grade). Methanol (HPLC grade) was purchased from Tedia (Fairfield, OH, USA). Formic acid (HPLC grade) was purchased from Aladdin (Shanghai, China). Ultrapure water was prepared using a Milli-Q system (Millipore, USA). Sodium formate and leucine enkephalin were obtained from Waters (Milford, USA). Dulbecco's minimum essential medium (DMEM) was purchased from Gibco (CA, USA). Fetal bovine serum (FBS) was supplied by Clark Biotechnology Institution (Richmond, VA, USA). 3-(4,5-Dimethylthiazol-2-yl)-2,5-diphenyltetrazolium bromide (MTT) and lipopolysaccharides (LPS) were obtained from Solarbio (Beijing, China). Dimethyl sulfoxide (DMSO) was bought from Macklin Biochemical Co., Ltd. (Shanghai, China). Mouse TNF-α and IL-6 ELISA kits were obtained from Huangshi Yanke Biotechnology Co., Ltd. (Hubei, China). The Enhanced BCA Protein Assay Kit, RIPA Lysis Buffer, Phenylmethylsulfonyl Fluoride (PMSF), Primary Antibody Dilution Buffer, Secondary Antibody Dilution Buffer, Blocking Buffer, and Western Wash Buffer were obtained from Beyotime Biotechnology (Shanghai, China). The hypersensitivity enhanced chemiluminescence (ECL) substrate kit was purchased from Beijing Labgic Technology Co., Ltd. (Beijing, China). Rabbit polyclonal antibodies of STAT3 (10253–2-AP), NF-κB p65 (10745–1-AP), β-actin (20536–1-AP), and HRP-conjugated Affinipure Goat Anti-Rabbit IgG (H + L) (SA00001-2) were purchased from Proteintech Group (Wuhan, China). Rabbit anti-Phospho-STAT3 (P-STAT3) (AF3293) and Phospho-NF-κB p65 (P-p65) (AF2006) were obtained from Affinity Biosciences (Jiangsu, China). All other chemicals and organic solvents were of analytical grade or better.

2.2. Extractions

1.5 g of THJGW powder was accurately weighed and placed in a 50 mL conical flask with stopper. Then, 50 mL of methanol was precisely measured and added to dissolve, then the flask was re-weighed to determine its mass. After ultrasound extracted (40 kHz, 100 W) for 1 h, any weight loss was compensated by adding methanol. The resulting mixture was shaken and filtered, then 1 mL of the filtrate was precisely transferred to a 50 mL volumetric flask with the volume set to the mark. Before analysis, the prepared solution was filtered through a 0.22 μm microporous membrane filter.

2.3. Animals handling

15 male Sprague-Dawley rats (180–220 g) were supplied by Liaoning Changsheng Biotechnology Co., Ltd. (Dalian, China). All rats were housed in a controlled environment (12 h light/dark cycle, temperature: 25 ± 1 ℃, relative humidity: 50 ± 5 %) with freely available food and water. After 7 days of adaptive feeding, the rats were randomly divided into five groups of three. One group was designated as the control group. Rats were given THJGW powder (3.0 g/kg/d) via gavage for 7 days, while the control group received the same amount of saline. All animal experiments were approved by the Bioethics Committee of Changchun University of Chinese Medicine and performed in accordance with the guidelines of the Institutional Animal Care (Approval No. 2023452).

2.4. Serum collection and preparation

Prior to the day of last administration, the rats were fasted for 12 h with only access to water. Abdominal aortic blood samples were collected at 0.25, 0.5, 1, and 2 h after the last dose. These samples were then clotted for 30 min at room temperature before being centrifuged at 3000 rpm for 10 min at 4 °C. The resulting serum samples were then divided into smaller aliquots and stored at −80 °C until further analysis.

At each time point, 900 μL serum sample was collected and mixed with a four-fold volume of methanol. The mixture was vortexed for 2

min and then centrifuged at 3000 rpm for 10 min at 4 °C. The supernatant was collected and dried with nitrogen. The residue was then dissolved in 100 μL of methanol. Finally, the solution was centrifuged at 13000 rpm for 10 min at 4 °C before injecting 2 μL of the supernatant for UPLC-Q-TOF-MS analysis.

2.5. UPLC-MS analysis

A Waters Acquity UPLC system equipped with a Q-TOF SYNAPT G2-Si HDMS mass spectrometer (Waters, USA) was utilized to analyze the in *vitro* and in *vivo* (absorbed in blood) chemical components of THJGW. A Supelco Ascentis® Express C18 Column (2.7 μm, 3.0 × 50 mm) was used at 40 °C with 0.1 % (v/v) formic acid in water (A) and 0.1 % (v/v) formic acid in methanol (B) as mobile phase. The gradient elution conditions for positive ion mode were as follows: 0–2 min, 10–32 % B; 2–3 min, 32–65 % B; 3–5 min, 65–75 % B; 5–7 min, 75–85 % B; 7–12 min, 85–90 % B; 12–15 min, 90–95 % B; 15–17 min, 95 % B; 17–22 min, 95–10 % B; 22–25 min, 10 % B. And for negative ion mode, the gradient elution conditions were as follows: 0–2 min, 10–25 % B; 2–4 min, 25–32 % B; 4–8 min, 32–43 % B; 8–11 min, 43–65 % B; 11–13 min, 65–85 % B; 13–18 min, 85–90 % B; 18–21 min, 90–95 % B; 21–23 min, 95 % B; 23–28 min, 95–10 % B; 28–31 min, 10 % B. The flow rate was 0.4 mL/min and the injection volume was 2 μL for all the cases above. Specific and accurate masses of all samples in both positive and negative ion modes were determined using mass spectrometry with an electrospray ion source (ESI). The mass range was 50–2000 Da and a scan speed of 1.5 s was used in MS^E resolution mode. The temperature of ion source was 120 °C in positive ion mode and 110 °C in negative ion mode. The desolvation temperature was 400 °C. The flow rates for desolvation gas and cone gas were 800 and 50 L/h, respectively. The capillary voltage was set to 3.0 kV in the positive ion mode and 2.5 kV in the negative ion mode. The sampling cone voltage was 40 V. The low collision energy was 6 V, while the high collision energy was set to 20–30 V and 30–45 V for MS^E mode. Sodium formate was used in calibrating the mass spectrometer, and leucine enkephalin (m/z 556.2771 in positive ion mode, m/z 554.2615 in negative ion mode) was used as the lock mass.

2.6. Target network pharmacology

2.6.1. Screening for active component targets of THJGW

The prototype components absorbed in blood of THJGW were used as candidates. Their 2D structures were searched and downloaded from the PubChem compound database, and then component targets were predicted following the method of Zhao et al. (Zhao et al., 2023).

2.6.2. Acquisition of OA targets

Using “osteoarthritis” as the keyword, OA-related targets were retrieved following the method of Zhao et al. (Zhao et al., 2023). Then, components-related targets were intersected with OA-related targets and visualized by the OmicShare tools, a free online platform for data analysis (https://www.omicshare.com/tools) to identify potential targets for THJGW in the treatment of OA.

2.6.3. Protein–protein interaction network

Above intersection targets following the method of Zhao et al. were uploaded into the STRING database and Cytoscape 3.7.2 to visualize a protein–protein interaction (PPI) network (Zhao et al., 2023). Furthermore, the CytoHubba plug-in with the maximal clique centrality (MCC) algorithm was utilized to predict 10 probable hub genes of THJGW against OA.

2.6.4. Network construction

A complex “herbs-components-targets-disease” network was constructed in Cytoscape 3.7.2 following the method of Zhao et al. (Zhao et al., 2023). The network was later topologically analyzed by the CytoNCA plug-in to screen out the key components based on values of degree centrality (DC) and between centrality (BC).

2.6.5. GO enrichment analysis and KEGG enrichment analysis

Intersection targets were following the method of Zhao et al. submitted into the Metascape database for GO enrichment and KEGG pathway analysis to explore the core mechanisms and pathways of THJGW anti-OA (Zhao et al., 2023). GO enrichment analysis mainly includes biological processes (BP), cellular components (CC), and molecular functions (MF). Subsequently, the top 10 GO terms and top 20 KEGG pathways were screened, and the results were visualized on a bioinformatics network platform (https://www.bioinformatics.com) for GO analysis bar charts and KEGG pathway enrichment analysis bubble charts.

2.7. Molecular docking

Molecular docking was performed on key components predicted by degree centrality (DC) and between centrality (BC) values, as well as core targets obtained using the MCC algorithm. The 3D structures of compounds were downloaded in SDF format from the PubChem database and converted into MOL2 format using Open Babel software. The 3D crystal structures of targets VEGFA (PDB ID: 1MKK), STAT3 (PDB ID: 6NJS), RELA/NF-κB p65 (PDB ID: 3QXY), PIK3R1 (PDB ID: 1PBW), PIK3CA (PDB ID: 6GVF), MMP9 (PDB ID: 1ITV), MMP1 (PDB ID: 1CGE), IL-6 (PDB ID: 1ALU), HDAC1 (PDB ID: 4BKX), and FGF2 (PDB ID: 1BAS) were retrieved from the Research Collaboratory for Structural Bioinformatics (RCSB) Protein Data Bank (PDB) database (https://www.rcsb.org/). All protein and ligand structures were pre-processed using AutoDockTools 1.5.6 and saved as a PDBQT format file. The docking simulation was performed with AutoDock Vina 1.1.2 to estimate the potential binding modes between active compounds and core targets. The 2D and 3D structures of the ligands and targets with a high binding score were visualized by Discovery Studio software, and the heatmap for binding affinity of molecular docking was plotted on a bioinformatics network platform (http://www.bioinformatics.com).

2.8. Cell culture and viability assay

The RAW264.7 murine macrophage cell line was obtained from iCell Bioscience Inc. (Shanghai, China) and cultured with DMEM containing 10 % FBS at 37 °C in a 5 % CO_2 humidified incubator.

Cells (1×10^4 cells/well) were seeded into 96-well plates and incubated for 24 h. Then, cells were treated with increasing concentrations of LPS (0.25, 0.5, 1, 2, 5, 10 μg/mL) and THJGW (6.25, 12.5, 25, 50, 100, 200 μg/mL) alone for 24 h, followed by 1 μg/mL of LPS was used to be co-treated with THJGW for 24 h. Cells untreated with LPS and THJGW were considered the control group. 50 μL of MTT solution (2 mg/mL) was added to each well, followed by cultivation for 3 h. The formaldehyde crystals formed were dissolved in 200 μL of DMSO after removing MTT, and the absorbance of the solutions was measured at 490 nm with a microplate reader.

2.9. ELISA of TNF-α and IL-6

RAW264.7 cells (2×10^5 cells/well) were inoculated on 6-well plates and cultured for 24 h. After pre-treatment by THJGW for 1 h, cells were stimulated with 1 μg/mL LPS for 24 h. Subsequently, the cell supernatant was collected, and the concentrations of TNF-α and IL-6 in the culture supernatant were determined using the appropriate ELISA kits according to the manufacturer’s instructions.

2.10. Western blot

RAW264.7 cells were seeded in 6-well plates at a density of 2×10^5 cells/well and treated with a combination of 1 μg/mL LPS and THJGW at varying concentrations for 24 h. Cells were harvested and fully lysed

with the RIPA lysis buffer containing 1 % PMSF at 0 °C, followed by collecting supernatants. The protein concentration of lysates was measured using the BCA protein assay kit. Equal amounts of protein samples were separated using 12.5 % sodium dodecyl sulfate–polyacrylamide gel electrophoresis (SDS-PAGE) and transferred to polyvinylidene difluoride (PVDF) membranes. The membranes were blocked in the blocking buffer for 1.5 h at room temperature before being incubated with the primary antibody at 4 °C overnight in a shaking incubator. The primary antibodies used were diluted as follows: STAT3 (1:2000), NF-κB p65 (1:1000), P-STAT3 (1:1000), P-p65 (1:1000), and β-actin (1:1000). The membranes were washed three times with the wash buffer before incubating with the HRP-conjugated secondary antibody (1:4000) for 50 min at room temperature. After three washes, the blots were visualized using the hypersensitivity ECL substrate kit. Then, the images were captured on a Tanon 5200 chemiluminescence imaging system (Shanghai, China) and analyzed with Image J software.

3. Results

3.1. Identification of main constituents of THJGW

The high-resolution mass spectrometry data of THJGW were rapidly acquired using the UPLC-Q-TOF-MS^E method equipped with MassLynx V4.1 software, and the base peak ion (BPI) chromatograms of THJGW in positive and negative ion modes are shown in Fig. 1. The prototype library of UNIFI platform has been enriched with literature, ChemSpider, and SciFinder Scholar to interpret each liquid peak. A total of 134 components including flavonoids, iridoid glycosides, phenylethanoid glycosides, phenylpropanoids, organic acids, phenolics, and other compounds in THJGW were inferred and identified via the UNIFI platform, comparison with standards, references from the literature, and the cleavage laws of mass spectrometry. Detailed mass spectrometry informations on these compounds are shown in Table 1. The chemical structures of the main compounds were summarized in Fig. 2 based on accurate molecular mass, mass spectrometry data, and relevant literature.

3.1.1. Flavonoids

In this study, a total of 45 flavonoids including flavonoid O-glycosides and flavonoid aglycones were identified in both positive and negative ion modes in THJGW. The main sources of flavonoids were Epimedium brevicornum, followed by Spatholobus, Rhizoma drynariae, and Pyrola.

37 flavonoid O-glycosides were characterized in the mass spectrum of THJGW. They were divided into two categories: 8-prenyl flavonoid O-glycosides and flavonoid O-glycosides without isopentenyl groups, according to the presence of isopentenyl at the C-8 position in their structures. Glycosidic bonds connected by the oxygen atom in flavonoid O-glycosides were cleaved in both positive and negative ion modes, which were characterized mostly by the neutral losses of 162 Da (Glc), 146 Da (Rha), and 132 Da (Xyl).

3.1.1.1. 8-Prenyl flavonoid O-glycosides. 8-Prenyl flavonoid O-glycosides derived from Epimedium brevicornum show similar fragmentation patterns in mass spectrometry. First, in positive ion mode, the cleavage pathway typically involves losing the C-3 position of an O-substituted diglycosyl or one of them. Second, the loss of the C-7 position of an O-substituted or the C-3 position of the remaining glycosyl to generate anhydroicaritin. Finally, the prenyl group at the C-8 position was lost. In negative ion mode, firstly, cleavage starts with the loses the C-7 position of the O-substituted glycosyl group, followed by the C-3 position of the O-substituted diglycosyl, and finally the prenyl group at the C-8 position was lost. The following describes the identification process for several representative compounds.

Compounds 47, 48, 51, and 55 separately showed molecular ion peaks at *m/z* 839.2960, 809.2860, 823.3024, and 677.2441 for $[M + H]^+$ in positive ion mode. The loss of a molecule glycosyl group was observed to generate fragment ions at *m/z* 677 in compounds 47, 48, and 51, which were corresponding to $[M + H\text{-Glc}]^+$, $[M + H\text{-Xyl}]^+$, and $[M + H\text{-Rha}]^+$, respectively. Compounds 47, 48, 51, and 55 showed similar characteristic fragment ions at *m/z* 531, 369, and 313. Ions at *m/z* 531 were separately corresponding to $[M + H\text{-Rha-Glc}]^+$, $[M + H\text{-Rha-Xyl}]^+$, $[M + H\text{-2Rha}]^+$, and $[M + H\text{-Rha}]^+$. Then they separately lost a glucosyl group to generate anhydroicaritin at *m/z* 369. Ions at *m/z* 313 were the losses of the C_4H_8 group, corresponding to $[M + H\text{-Rha-2Glc-isobutenyl}]^+$, $[M + H\text{-Rha-Xyl-Glc-isobutenyl}]^+$, $[M + H\text{-2Rha-Glc-isobutenyl}]^+$, and $[M + H\text{-Rha-Glc-isobutenyl}]^+$, respectively. Likewise, fragment ions at *m/z* 367, 366, 352, 351, and 323 with similar cleavage pathways to positive mode for compounds 47, 48, 51, and 55 were observed in negative ion mode, also including losses of neutral molecules such as CH_3 and CO_2. According to the UNIFI data matching and the cleavage pathways, compounds 47, 48, 51, and 55 were identified as hexandraside F, epimedin B, epimedin C, and sagittatoside A, respectively. Furthermore, compounds 41, 42, and 64 exhibited similar fragmentation pathways with them in the mass spectrum, and in combination with accurate masses, they were identified as diphylloside A, sagittasine C, and baohuoside II respectively.

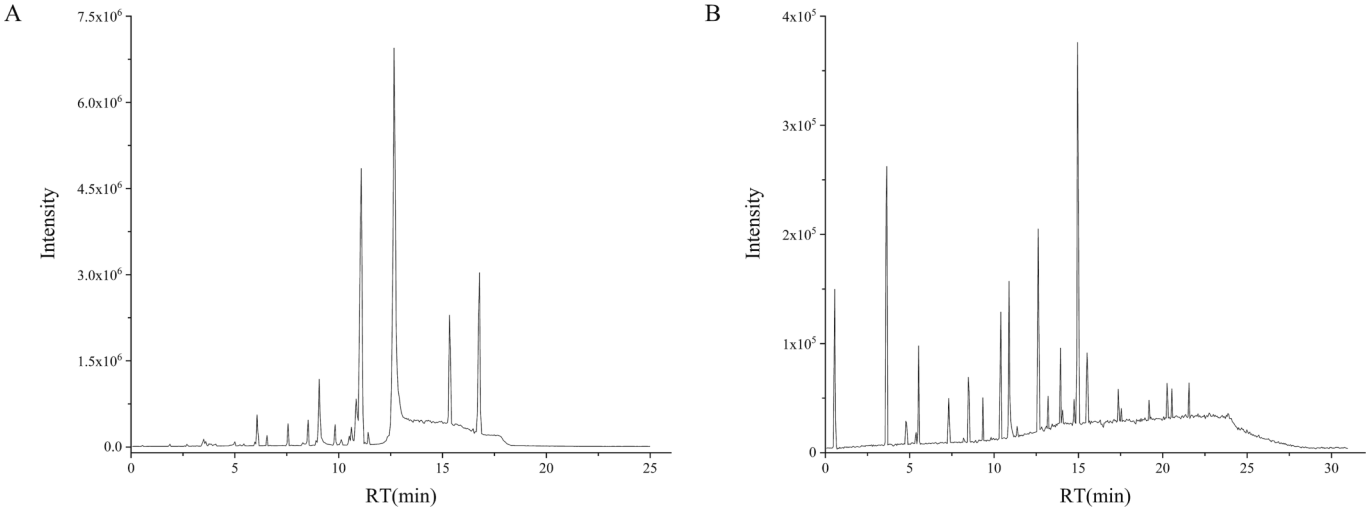

Fig. 1. Base peak ion chromatograms of THJGW in positive ion mode (A) and negative ion mode (B).

Table 1
Identification of chemical constituents from THJGW by UPLC-Q-TOF-MS.

NO.	Identified	Selected ion	RT (min)	Formula	Measured mass (*m/z*)	Mass error (ppm)	Major product ions	Type	Attribution
P1	Melibiose	$[M-H]^-$	0.56	$C_{12}H_{22}O_{11}$	341.1084	−1.5	221.0663,179.0559	Other compounds	a
P2	Glucose	$[M-H]^-$	0.56	$C_6H_{12}O_6$	179.0551	−5.7	161.0448,89.0242	Other compounds	a,d
P3	Mannitol	$[M-H]^-$	0.56	$C_6H_{14}O_6$	181.0710	−3.9	149.0450,119.0345	Other compounds	d
P4	Quinic acid	$[M-H]^-$	0.56	$C_7H_{12}O_6$	191.0558	−1.7	173.0448,128.0434,85.0287,71.0133,59.0141	Organic acids	e
P5	5-GGMF	$[M+HCOO]^-$	0.57	$C_{18}H_{26}O_{13}$	495.1345	−2.2	161.0451,125.0242	Other compounds	a
P6	Citric acid	$[M-H]^-$	0.58	$C_6H_8O_7$	191.0194	−1.5	173.0033,87.0087	Organic acids	a,d,e
P7	Glucoraphenin	$[M-H]^-$	0.60	$C_{12}H_{21}NO_{10}S_3$	434.0243	−2.8	383.1189,179.0559	Other compounds	g
P8	Kankanoside B	$[M+HCOO]^-$	0.63	$C_{15}H_{24}O_{10}$	409.1353	0.3	183.0625,165.0786,101.0240,71.0140	Iridoid glycosides	d
P9	Koaburaside	$[M-H]^-$	1.05	$C_{14}H_{20}O_9$	331.1038	1.0	179.0560	Phenolics	f
P10	Rehmannioside D	$[M+HCOO]^-$	1.06	$C_{27}H_{42}O_{20}$	731.2251	−0.1	541.1209,179.0560	Iridoid glycosides	a
P11	Acetylcatalpol	$[M+HCOO]^-$	1.07	$C_{18}H_{26}O_{10}$	447.1513	1.1	179.0560	Iridoid glycosides	a
P12	Geniposidic acid	$[M-H]^-$	1.44	$C_{16}H_{22}O_{10}$	373.1133	−2.0	211.0568,193.0480,149.0628	Iridoid glycosides	a,d
P13	Androsin	$[M+HCOO]^-$	1.44	$C_{15}H_{20}O_8$	373.1133	−2.0	149.0608	Phenolics	b
P14	Protocatechuic acid	$[M-H]^-$	1.44	$C_7H_6O_4$	153.0194	0.3	149.0608,101.0318	Organic acids	a,b,c,e,f
P15	Kankanose	$[M-H]^-$	1.64	$C_{27}H_{38}O_{18}$	649.1983	−0.4	485.1235,179.0347,135.0449	Other compounds	d
P16	6-O-Caffeoylglucopyranose	$[M-H]^-$	1.69	$C_{15}H_{18}O_9$	341.0871	−2.2	179.0347,135.0449	Phenylpropanoids	a
P17	Caffeic acid	$[M-H]^-$	1.71	$C_9H_8O_4$	179.0347	−1.4	135.0449,113.0242	Organic acids	a,c,e,g
P18	Decaffeoyl acteoside	$[M-H]^-$	1.73	$C_{20}H_{30}O_{12}$	461.1660	−0.9	179.0342,135.0449	Phenylethanoid glycosides	a,d
P19	3-O-sinapicoylquinic acid	$[M+H]^+$	1.74	$C_{18}H_{22}O_{10}$	399.1268	−4.4	369.1153,251.0916	Organic acids	g
P20	Cistanoside F or its isomer	$[M-H]^-$	1.83	$C_{21}H_{28}O_{13}$	487.1452	−1.0	294.1338,179.0356	Phenylethanoid glycosides	a,d
P21	Salidroside	$[M+HCOO]^-$	1.87	$C_{14}H_{20}O_7$	345.1178	−3.7	294.1338,264.0889	Phenylethanoid glycosides	d
P22	6-Deoxycatalpol	$[M+HCOO]^-$	1.91	$C_{15}H_{22}O_9$	391.1251	1.3	264.0889	Iridoid glycosides	d
P23	8-Epiloganic acid	$[M-H]^-$	1.94	$C_{16}H_{24}O_{10}$	375.1289	−2.0	294.1338,264.0889	Iridoid glycosides	a,d
P24	Mussaenosidic acid	$[M-H]^-$	1.94	$C_{16}H_{24}O_{10}$	375.1289	−2.0	294.1338,264.0889	Iridoid glycosides	d
P25	6-O-Feruloylajugol	$[M+HCOO]^-$	1.97	$C_{25}H_{32}O_{12}$	569.1868	−1.4	407.1330,294.1338	Phenylpropanoids	a
P26	Kankanoside E	$[M+H]^+$ $[M-H]^-$	2.32 6.55	$C_{16}H_{28}O_8$	349.1837 347.1707	−5.7 −1.2	179.0340 329.1520,167.0670	Other compounds	d
P27	Sibirioside B	$[M+HCOO]^-$	2.40	$C_{22}H_{30}O_{13}$	547.1673	0.8	179.0346	Phenylpropanoids	a
P28	Cistanoside F or its isomer	$[M-H]^-$	2.51	$C_{21}H_{28}O_{13}$	487.1458	0.3	251.0576,179.0346	Phenylethanoid glycosides	a,d
P29	5,7-Dihydroxychromone-7-O-rutinoside	$[M-H]^-$	2.67	$C_{21}H_{26}O_{13}$	485.1294	−1.3	177.0191	Phenylpropanoids	c
P30	Gluroside	$[M+HCOO]^-$	2.68	$C_{15}H_{24}O_8$	377.1451	−0.6	177.0191	Iridoid glycosides	d
P31	Cistantubuloside C1/C2	$[M-H]^-$	2.75	$C_{35}H_{46}O_{21}$	801.2470	1.4	623.2148,179.0347	Phenylethanoid glycosides	d
P32	Forsythoside B	$[M+HCOO]^-$	2.75	$C_{34}H_{44}O_{19}$	801.2470	1.4	179.0347	Phenylethanoid glycosides	a
P33	Darendoside B	$[M-H]^-$	2.81	$C_{21}H_{32}O_{12}$	475.1824	0.6	461.1674,375.1435	Phenylethanoid glycosides	a
P34	7,8,3′,4′-Tetrahydroxyflavanone	$[M+H]^+$	3.03	$C_{15}H_{12}O_6$	289.0709	0.9	204.9809,163.0389	Flavonoids	f

(*continued on next page*)

Table 1 (*continued*)

NO.	Identified	Selected ion	RT (min)	Formula	Measured mass (*m*/*z*)	Mass error (ppm)	Major product ions	Type	Attribution
P35	Neoeriocitrin	$[M+H]^+$	3.04	$C_{27}H_{32}O_{15}$	597.1817	0.5	525.2881,289.0723,163.0389	Flavonoids	c
		$[M-H]^-$	4.36		595.1665	−0.7	459.1137,235.0245,151.0030		
P36	Naringenin-7-O-glucoside	$[M+H]^+$	3.18	$C_{21}H_{22}O_{10}$	435.1285	−0.3	273.0763,153.0181	Flavonoids	c
P37	Liquiritin	$[M+H]^+$	3.19	$C_{21}H_{22}O_9$	419.1346	2.3	332.0912,228.1596	Flavonoids	c,e
P38	Naringenin	$[M+H]^+$	3.19	$C_{15}H_{12}O_5$	273.0759	0.6	153.0181,147.0442,119.0492	Flavonoids	f
P39	Naringin	$[M+H]^+$	3.19	$C_{27}H_{32}O_{14}$	581.1882	3.0	435.3332,273.0763,153.0181	Flavonoids	c
		$[M-H]^-$	5.36		579.1712	−1.2	271.0607,151.0033		
P40	Campneoside II or its isomer	$[M-H]^-$	3.27	$C_{29}H_{36}O_{16}$	639.1932	0.3	621.1796,593.1485,161.0240	Phenylethanoid glycosides	a,d
P41	Diphylloside A	$[M+H]^+$	3.45	$C_{38}H_{48}O_{20}$	825.2789	−2.8	663.2299,517.1704,355.1180,299.0554	Flavonoids	e
P42	Sagittasine C	$[M+H]^+$	3.52	$C_{33}H_{40}O_{16}$	693.2354	−5.0	547.1799,385.1280,329.0650	Flavonoids	e
P43	Echinacoside	$[M-H]^-$	3.62	$C_{35}H_{46}O_{20}$	785.2506	−0.4	623.2188,461.1660,179.0347,161.0240	Phenylethanoid glycosides	a,d
P44	Purpureaside C	$[M-H]^-$	3.62	$C_{35}H_{46}O_{20}$	785.2506	−0.4	623.2188,179.0347,161.0240,133.0291	Phenylethanoid glycosides	a
P45	Kankanoside F	$[M-H]^-$	3.62	$C_{26}H_{40}O_{17}$	623.2199	1.1	477.1605,461.1660,179.0347,161.0240	Phenylethanoid glycosides	d
P46	Acuminatoside	$[M+H]^+$	3.69	$C_{45}H_{60}O_{24}$	985.3565	1.8	831.2673,673.2218,285.0762	Flavonoids	e
P47	Hexandraside F	$[M+H]^+$	3.72	$C_{39}H_{50}O_{20}$	839.2960	−1.0	677.2450,531.1863,369.1334,313.0706	Flavonoids	e
		$[M+HCOO]^-$	10.15		883.2865	−1.4	675.2296,366.1104,351.0870,323.0926		
P48	Epimedin B	$[M+H]^+$	3.74	$C_{38}H_{48}O_{19}$	809.2860	−0.3	677.2450,531.1863,369.1334,313.0708	Flavonoids	e
		$[M+HCOO]^-$	10.20		853.2767	−0.6	645.2182,366.1104,351.0870,323.0926		
P49	2-phenylethyl-β-primeveroside	$[M-H]^-$	3.76	$C_{19}H_{28}O_{10}$	415.1589	−4.9	191.0560	Phenylethanoid glycosides	a
P50	Renifolin	$[M+H]^+$	3.77	$C_{23}H_{34}O_8$	439.2318	−1.9	369.1334,85.0285	Phenolics	b
P51	Epimedin C	$[M+H]^+$	3.78	$C_{39}H_{50}O_{19}$	823.3024	0.6	677.2450,531.1863,369.1334,313.0708	Flavonoids	e
		$[M+HCOO]^-$	10.42		867.2923	−0.6	659.2344,513.1762,366.1105,351.0865,323.0925		
P52	Demethyl syringin	$[M-H]^-$	3.79	$C_{16}H_{22}O_9$	357.1187	−1.1	177.0550	Phenylpropanoids	d
P53	Icariside I	$[M+H]^+$	3.79	$C_{27}H_{30}O_{11}$	531.1861	0.0	369.1334,313.0708	Flavonoids	e
		$[M-H]^-$	12.13		529.1706	−1.8	367.1177,352.0929		
P54	Korepimedoside A	$[M+H]^+$	3.80	$C_{37}H_{44}O_{17}$	761.2619	−4.3	531.1863,369.1334,313.0708	Flavonoids	e
P55	Sagittatoside A	$[M+H]^+$	3.80	$C_{33}H_{40}O_{15}$	677.2441	0.0	531.1862,369.1334,313.0706	Flavonoids	e
		$[M-H]^-$	12.44		675.2291	−0.5	367.1176,352.0938		
P56	Jionoside A1/A2	$[M-H]^-$	4.03	$C_{36}H_{48}O_{20}$	799.2643	−2.9	623.2190,135.0449	Phenylethanoid glycosides	a
P57	Cistanoside A	$[M-H]^-$	4.03	$C_{36}H_{48}O_{20}$	799.2643	−2.9	623.2190,399.1288,219.0656	Phenylethanoid glycosides	d
P58	Campneoside II or its isomer	$[M-H]^-$	4.08	$C_{29}H_{36}O_{16}$	639.1924	−1.1	621.1798,399.1288,219.0656	Phenylethanoid glycosides	a,d
P59	Rehmapicrogenin	$[M-H]^-$	4.19	$C_{10}H_{16}O_3$	183.1026	−0.1	139.1136	Other compounds	a
P60	Kankanoside K1/K2	$[M-H]^-$	4.29	$C_{36}H_{48}O_{21}$	815.2621	0.7	784.2413,769.2551	Phenylethanoid glycosides	d
P61	8-Prenylkaempferol	$[M+H]^+$	4.32	$C_{20}H_{18}O_6$	355.1178	0.5	299.0553,208.0328,191.0011	Flavonoids	e
		$[M-H]^-$	12.57		353.1025	−1.7	323.0921,295.0614		
P62	Ligupurpuroside A	$[M-H]^-$	4.33	$C_{35}H_{46}O_{19}$	769.2555	−0.7	623.2181,595.1662,459.1136	Phenylethanoid glycosides	a
P63	Poliumoside	$[M-H]^-$	4.33	$C_{35}H_{46}O_{19}$	769.2555	−0.7	623.2181,595.1662,459.1136	Phenylethanoid glycosides	d
P64	Baohuoside II	$[M+H]^+$	4.33	$C_{26}H_{28}O_{10}$	501.1760	0.9	355.1174,299.0553,191.0011	Flavonoids	e
		$[M-H]^-$	11.65		499.1599	−2.2	352.0946,297.0392		

(*continued on next page*)

Table 1 (*continued*)

NO.	Identified	Selected ion	RT (min)	Formula	Measured mass (*m/z*)	Mass error (ppm)	Major product ions	Type	Attribution
P65	Dunnisinoside	$[M + HCOO]^-$	4.39	$C_{26}H_{30}O_{13}$	595.1659	−1.6	235.0247,151.0028	Iridoid glycosides	a
P66	Jionoside A1/A2	$[M-H]^-$	4.42	$C_{36}H_{48}O_{20}$	799.2648	−2.3	623.2184,595.1665,135.0449	Phenylethanoid glycosides	a
P67	Arenarioside	$[M-H]^-$	4.63	$C_{34}H_{44}O_{19}$	755.2378	−3.5	579.1307	Phenylethanoid glycosides	d
P68	Pinoresinol-β-D-glucoside	$[M-H]^-$	4.75	$C_{26}H_{32}O_{11}$	519.1866	−1.2	461.1649,357.1335,161.0241	Phenylpropanoids	d
P69	Acteoside	$[M-H]^-$	4.81	$C_{29}H_{36}O_{15}$	623.1976	−0.9	461.1649,315.1048,179.0355,161.0241	Phenylethanoid glycosides	a,d
P70	Tubuloside A	$[M-H]^-$	4.84	$C_{37}H_{48}O_{21}$	827.2607	−1.0	665.2281,623.1976,461.1649,161.0241	Phenylethanoid glycosides	d
P71	Hyperoside	$[M-H]^-$	4.89	$C_{21}H_{20}O_{12}$	463.0876	−1.4	300.0255,271.0232	Flavonoids	b,e
P72	Isoquercitrin	$[M-H]^-$	4.89	$C_{21}H_{20}O_{12}$	463.0876	−1.4	300.0255,285.0392,271.0232	Flavonoids	b,e,f
P73	Sagittatoside B	$[M + H]^+$	5.06	$C_{32}H_{38}O_{14}$	647.2339	0.7	563.3768,248.1323	Flavonoids	e
P74	2-O-Galloylhyperin	$[M-H]^-$	5.06	$C_{28}H_{24}O_{16}$	615.0978	−2.2	609.1450	Flavonoids	b
P75	2-O-Rhamnosylicariside II or its isomer	$[M + H]^+$	5.19	$C_{33}H_{40}O_{14}$	661.2493	0.3	369.1333,313.0709	Flavonoids	e
		$[M-H]^-$	10.42		659.2339	−0.9	513.1759,367.1175,351.0866,323.0920,296.0332		
P76	Syringaresinol-4-O-β-D-glucopyranoside	$[M-H]^-$	5.20	$C_{28}H_{36}O_{13}$	579.2085	0.3	417.1546	Phenylpropanoids	d
P77	Icaritin	$[M + H]^+$	5.22	$C_{21}H_{20}O_6$	369.1335	0.7	313.0709,135.0441	Flavonoids	e
		$[M-H]^-$	13.65		367.1181	−1.5	352.0958,309.0399,297.0407		
P78	Jionoside B1/B2	$[M-H]^-$	5.29	$C_{37}H_{50}O_{20}$	813.2818	−0.6	579.1715,459.1140	Phenylethanoid glycosides	a
P79	Rehmapicroside	$[M-H]^-$	5.45	$C_{16}H_{26}O_8$	345.1543	−3.4	161.0238,135.0446	Other compounds	a
P80	Kankanoside A	$[M-H]^-$	5.45	$C_{16}H_{26}O_8$	345.1543	−3.4	161.0242	Iridoid glycosides	d
P81	Isomer of acteoside	$[M-H]^-$	5.54	$C_{29}H_{36}O_{15}$	623.1973	−1.3	461.1660,315.1009,179,0326,161.0242	Phenylethanoid glycosides	a,d
P82	Forsythiaside A	$[M-H]^-$	5.54	$C_{29}H_{36}O_{15}$	623.1973	−1.3	461.1660,315.1078,161.0242	Phenylethanoid glycosides	a,d
P83	3, 6-Disinapoyl sucrose	$[M-H]^-$	5.59	$C_{34}H_{42}O_{19}$	753.2248	0.0	223.0604,205.0503,190.0266	Other compounds	g
P84	Campneoside I or its isomer	$[M-H]^-$	5.60	$C_{30}H_{38}O_{16}$	653.2104	2.6	623.1973,621.1834,461.1660,161.0242	Phenylethanoid glycosides	a,d
P85	Afrormosin	$[M + H]^+$	5.63	$C_{17}H_{14}O_5$	299.0912	−0.5	193.0494	Flavonoids	f
P86	Kankanoside G	$[M-H]^-$	5.66	$C_{29}H_{36}O_{14}$	607.2024	−1.4	461.1660	Phenylethanoid glycosides	d
P87	Kankanoside H1/H2	$[M-H]^-$	5.70	$C_{37}H_{48}O_{20}$	811.2663	−0.4	665.2288	Phenylethanoid glycosides	d
P88	Cistanoside C	$[M-H]^-$	5.97	$C_{30}H_{38}O_{15}$	637.2122	−2.5	564.4120,511.3497	Phenylethanoid glycosides	d
P89	Campneoside I or its isomer	$[M-H]^-$	6.02	$C_{30}H_{38}O_{16}$	653.2080	−1.1	637.2144,621.1840,461.1664	Phenylethanoid glycosides	a,d
P90	Kaempferol-3,7-O-rhamnoside	$[M-H]^-$	6.23	$C_{27}H_{30}O_{14}$	577.1557	−1.0	431.0953	Flavonoids	e
P91	Kankanoside I	$[M-H]^-$	6.41	$C_{35}H_{46}O_{18}$	753.2606	−0.7	607.2021	Phenylethanoid glycosides	d
P92	Leucosceptoside A	$[M-H]^-$	6.95	$C_{30}H_{38}O_{15}$	637.2127	−1.8	564.4120,315.1096	Phenylethanoid glycosides	a
P93	Syringaresinol	$[M-H]^-$	6.99	$C_{22}H_{26}O_8$	417.1545	−2.3	387.1112,181.0510	Phenylpropanoids	d,f
P94	Tubuloside B	$[M-H]^-$	7.23	$C_{31}H_{38}O_{16}$	665.2084	−0.4	461.1655,161.0240	Phenylethanoid glycosides	d
P95	2′-Acetylacteoside	$[M-H]^-$	7.26	$C_{31}H_{38}O_{16}$	665.2081	−0.9	503.1782,461.1654,161.0241	Phenylethanoid glycosides	a,d
P96	Jiocarotenoside A1/A2	$[M-H]^-$	7.32	$C_{21}H_{34}O_9$	429.2121	−2.1	174.9559,161.0241,112.9860	Other compounds	a
P97	Martynoside or its isomer	$[M-H]^-$	7.73	$C_{31}H_{40}O_{15}$	651.2289	−0.8	591.2077,175.0398	Phenylethanoid glycosides	a

(*continued on next page*)

Table 1 (*continued*)

NO.	Identified	Selected ion	RT (min)	Formula	Measured mass (*m/z*)	Mass error (ppm)	Major product ions	Type	Attribution
P98	Cistanoside D or its isomer	$[M-H]^-$	7.73	$C_{31}H_{40}O_{15}$	651.2289	−0.8	591.2077	Phenylethanoid glycosides	d
P99	Ikarisoside B or its isomer	$[M-H]^-$	8.15	$C_{32}H_{38}O_{15}$	661.2134	−0.6	352.0946,297.0394	Flavonoids	e
P100	Rouhuoside	$[M-H]^-$	8.20	$C_{38}H_{48}O_{20}$	823.2663	−0.4	661.2130,631.2026	Flavonoids	e
P101	Epimedoside E	$[M-H]^-$	8.25	$C_{37}H_{46}O_{19}$	793.2561	0.0	631.2026	Flavonoids	e
P102	Epimedoside A	$[M-H]^-$	8.43	$C_{32}H_{38}O_{15}$	661.2132	−1.0	514.1472,499.1582,353.1021	Flavonoids	e
P103	Diphylloside B	$[M-H]^-$	8.63	$C_{38}H_{48}O_{19}$	807.2722	0.6	645.2186,514.1480	Flavonoids	e
P104	Cistanoside D or its isomer	$[M-H]^-$	8.64	$C_{31}H_{40}O_{15}$	651.2304	1.5	529.1719,514.1480	Phenylethanoid glycosides	d
P105	Martynoside or its isomer	$[M-H]^-$	8.67	$C_{31}H_{40}O_{15}$	651.2281	−2.1	529.1719,514.1480	Phenylethanoid glycosides	a
P106	Elycohol-7-O-glucoside	$[M+H]^+$	8.89	$C_{21}H_{22}O_{11}$	451.1250	3.3	207.0323	Flavonoids	c
P107	Cistansinenside A	$[M-H]^-$	9.67	$C_{32}H_{40}O_{16}$	679.2236	−1.1	673.2147,353.1019	Phenylethanoid glycosides	d
P108	Cuhuoside	$[M+HCOO]^-$	9.81	$C_{33}H_{40}O_{16}$	737.2319	2.8	529.1731	Flavonoids	e
P109	Icariin	$[M+HCOO]^-$	10.37	$C_{33}H_{40}O_{15}$	721.2343	−0.8	513.1759,367.1175,351.0866,323.0920,296.0332	Flavonoids	e
P110	Curcumin	$[M-H]^-$	10.37	$C_{21}H_{20}O_6$	367.1180	−2.0	338.1142,217.0499	Other compounds	c
P111	Isomer of icariside II	$[M-H]^-$	10.38	$C_{27}H_{30}O_{10}$	513.1763	−0.7	367.1176,352.0934,324.1005	Flavonoids	e
P112	Epicatechin gallate	$[M-H]^-$	10.59	$C_{22}H_{18}O_{10}$	441.0817	−2.2	121.0296	Flavonoids	b
		$[M+H]^+$	16.48		443.0976	0.8	237.0794,207.0325		
P113	Paulownin	$[M-H]^-$	10.98	$C_{20}H_{18}O_7$	369.0967	−3.4	341.1027	Phenylpropanoids	a
P114	Anhydroicaritin-3-O- rhamnopyranosyl(4 → 1)-furan acid-7-O-glucopyranoside	$[M-H]^-$	11.02	$C_{39}H_{48}O_{19}$	819.2712	−0.6	657.2176,367.1180	Flavonoids	e
P115	3,4-Dihydroxyacetophenone	$[M+H]^+$	11.09	$C_8H_8O_3$	153.0547	0.3	135.0438,121.0284,93.0334	Phenolics	a
P116	Dibutyl phthalate	$[M+H]^+$	11.09	$C_{16}H_{22}O_4$	279.1591	0.1	149.0233	Other compounds	c
P117	Ikarisoside B or its isomer	$[M-H]^-$	11.38	$C_{32}H_{38}O_{15}$	661.2139	0.1	481.1487,352.0946	Flavonoids	e
P118	Rhein	$[M+HCOO]^-$	11.40	$C_{15}H_8O_6$	329.0289	−4.1	267.0486,211.1332	Other compounds	f
P119	Ikarisoside F	$[M-H]^-$	11.52	$C_{31}H_{36}O_{14}$	631.2037	0.7	571.1821,437.1605	Flavonoids	e
P120	2-O-Rhamnosylicariside II or its isomer	$[M-H]^-$	12.62	$C_{33}H_{40}O_{14}$	659.2335	−1.6	513.1760,367.1165,351.0869,323.0920,296.0324	Flavonoids	e
P121	Breviflavone A	$[M-H]^-$	12.66	$C_{25}H_{26}O_7$	437.1595	−2.3	281.0423	Flavonoids	e
P122	Icariside II	$[M-H]^-$	12.68	$C_{27}H_{30}O_{10}$	513.1760	−1.2	367.1164,352.0912,324.0966	Flavonoids	e
P123	Asiatic acid	$[M-H]^-$	12.91	$C_{30}H_{48}O_5$	487.3420	−1.8	471.3105,211.1334,167.1441	Organic acids	b
P124	Anhydroicaritin-3-O- rhamnopyranosyl-furan acid	$[M-H]^-$	13.03	$C_{33}H_{38}O_{14}$	657.2163	−4.0	367.1184,352.0943	Flavonoids	e
P125	Yinyanghuo B	$[M-H]^-$	13.70	$C_{25}H_{26}O_6$	421.1661	1.0	366.1085,311.1668,227.1074,211.0756	Flavonoids	e
P126	Spasuberoside A	$[M+HCOO]^-$	14.74	$C_{22}H_{25}O_9$	478.1508	5.8	433.1522	Flavonoids	f
P127	Linolenic acid	$[M-H]^-$	15.08	$C_{18}H_{30}O_2$	277.2171	−0.7	271.2276,165.1188	Organic acids	g
P128	Palmitic acid	$[M-H]^-$	16.48	$C_{16}H_{32}O_2$	255.2328	−0.8	223.0281	Organic acids	a,b,d,f,g
P129	Oleic acid	$[M-H]^-$	16.86	$C_{18}H_{34}O_2$	281.2478	−2.7	183.0115	Organic acids	b,g
P130	Juglanin	$[M+H]^+$	17.03	$C_{20}H_{18}O_{10}$	419.0956	−4.0	355.0701,221.0843	Flavonoids	b
P131	Stigmasterol	$[M+H]^+$	17.51	$C_{29}H_{48}O$	413.3779	0.3	360.3229,109.0645	Other compounds	c
P132	Stearic acid	$[M-H]^-$	18.43	$C_{18}H_{36}O_2$	283.2639	−1.2	231.9680	Organic acids	a,g
P133	Eleutheroside A	$[M+HCOO]^-$	21.08	$C_{35}H_{60}O_6$	621.4372	0.0	369.3371,323.3314	Other compounds	b,c,d,f
P134	Behenic acid	$[M-H]^-$	22.17	$C_{22}H_{44}O_2$	339.3267	−0.4	322.2127	Organic acids	a

a: Radix Rehmanniae Praeparata; b: Pyrola; c: Rhizoma Drynariae; d: Desertliving Cistanche; e: Epimedium brevicornum; f: Spatholobus; g: Radish Seed.

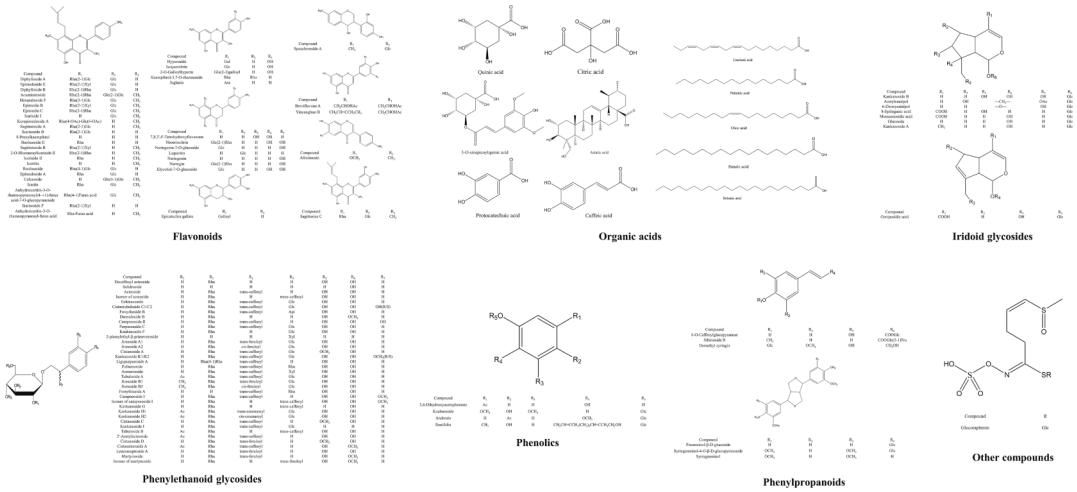

Fig. 2. Chemical structure of the main constitutions found in THJGW.

Compound 109 showed $[M + HCOO]^-$ at *m/z* 721.2343, and the main fragment ions at *m/z* 513.1759, 367.1175, 351.0866, 323.0920, and 296.0332, which were derived from losses of the glycosyl group and neutral molecules. Fragment ions at *m/z* 513.1759 and 367.1175 were separately corresponding to $[M-H-Glc]^-$ and $[M-H-Glc-Rha]^-$, and ions at *m/z* 351.0866, 323.0920, and 296.0332 were corresponding to $[M-H-Glc-Rha-CH_3-H]^-$, $[M-H-Glc-Rha-CH_3-H-CO]^-$, and $[M-H-Glc-Rha-CH_3-H-C_4H_7]^-$, respectively. Based on the literature reported (Chang et al., 2021), comparing the retention time and fragmentation pattern with the reference compound, compound 109 was identified as icariin, and its possible cleavage pathway in mass spectrometry is shown in Fig. 3.

Compounds 111 and 122 gave the $[M-H]^-$ ion at *m/z* 513, and the fragment ions at *m/z* 367, 352, and 324. The fragment ion at *m/z* 367 was the loss of a rhamnosyl group, corresponding to $[M-H-Rha]^-$. The ions at *m/z* 352 and 324 were generated by losing a molecule of methyl and carbon monoxide in a similar pathway, which were corresponding to $[M-H-Rha-CH_3]^-$ and $[M-H-Rha-CH_3-CO]^-$, respectively. By comparing the retention time and fragmentation pattern with the reference compound, compounds 111 and 122 were separately identified as isomer of icariside II and icariside II, and the possible cleavage pathway of icariside II in mass spectrometry is shown in Fig. S1.

3.1.1.2. Flavonoid O-glycosides without isopentenyl groups. The primary cleavage pattern in mass spectrometry of flavonoid O-glycosides without isopentenyl groups is the loss of glycosyl groups to generate a series of deglycosylated fragment ions, followed by a secondary bombardment of their aglycones.

Compound 36 gave a $[M + H]^+$ ion at *m/z* 435.1285, and the fragment ions at *m/z* 273.0763 and 153.0181. The fragment ion at *m/z* 273.0763 was corresponding to the loss of a molecule glucosyl as $[M + H\text{-}Glc]^+$. The ion at *m/z* 153.0181 was generated by the Retro-Diels-Alder (RDA) cleavage reaction of its aglycone. By comparison of the accurate mass and the cleavage pathways, compound 36 was identified as naringenin-7-O-glucoside.

Compound 39 showed $[M-H]^-$ at *m/z* 579.1712, and the fragment ions at *m/z* 271.0607 and 151.0033, which were separately corresponding to $[M-H-Rha-Glc]^-$ and $[M-H-Rha-Glc-C_8H_8O]^-$. The fragment ion at *m/z* 151.0033 was generated by the RDA cleavage reaction. Based on the accurate mass and compared with the standard, compound 39 was identified as naringin. In the same way, compound 71, with a similar cleavage pathway, was identified as hyperoside.

3.1.2. Iridoid glycosides

A total of 10 iridoid glycosides were inferred and identified from THJGW in the negative ion mode of mass spectrometry. Radix

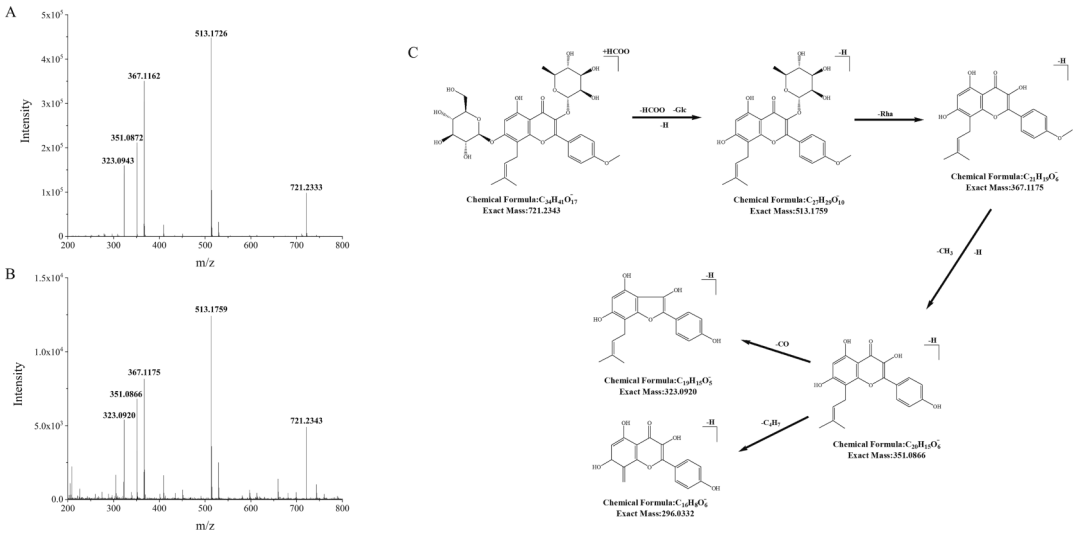

Fig. 3. MS/MS spectrum of icariin standard **(A)** and icariin **(B)**, as well as its possible cleavage pathway **(C)**.

Rehmanniae Praeparata and Desertliving Cistanche were the major sources of iridoid glycosides. These compounds shared a similar cleavage pathway in mass spectrometry, primarily cleavage of the glycosidic bond and the aglycone ring in negative ion mode, which was also associated with the loss of neutral molecules. Compound 12 was selected as an example to analyze and discuss the cleavage pathway of iridoid glycosides in mass spectrometry. Compound 12 showed $[M-H]^-$ at *m/z* 373.1133 and the fragment ions at *m/z* 211.0568, 193.0480, and 149.0628. The ion at *m/z* 211.0568 was generated by losing the glucosyl group, which was corresponding to $[M-H-Glc]^-$. The ions at *m/z* 193.0480 and 149.0628 were corresponding to the loss of a molecule water and carbon dioxide as $[M-H-Glc-H_2O]^-$ and $[M-H-Glc-H_2O-CO_2]^-$, respectively. According to the fragmentation pathways and standard comparison, compound 12 was identified as geniposidic acid, and its possible cleavage pathway in mass spectrometry is shown in Fig. S2.

3.1.3. Phenylethanoid glycosides

A total of 39 phenylethanoid glycosides were identified from THJGW in both positive and negative ion modes, with the majority coming from Radix Rehmanniae Praeparata and Desertliving Cistanche. In negative ion mode, these compounds typically cleave glycosidic and ester bonds, lose neutral glycosyl groups and phenylethanoid aglycones, or lose phenylpropene acyl groups and other small molecules. Positive ion mode typically results in the loss of neutral glycosyl groups, hydroxytyrosol (HT), and some neutral molecules usually occurs.

Compounds 69 and 81 showed the $[M-H]^-$ ion at *m/z* 623, and the fragment ions at *m/z* 461, 315, 179, and 161. Similar cleavage pathways were found in their mass spectrometry. The ions at *m/z* 461 and 315 were separately corresponding to $[M-H-caffeoyl]^-$ and $[M-H-caffeoyl-Rha]^-$. The ion at *m/z* 179 was corresponding to the loss of deprotonated caffeic acid as [caffeic acid-H]$^-$, and the ion at *m/z* 161 was caused by the loss of a molecule water, which was corresponding to [caffeic acid-H $-H_2O]^-$. By comparing the retention time and fragmentation pattern with the reference compound, compounds 69 and 81 were separately identified as acteoside and isomer of acteoside, and the possible cleavage pathway of acteoside in mass spectrometry is shown in Fig. 4.

Compound 43 showed $[M-H]^-$ at *m/z* 785.2506, and the fragment ions at *m/z* 623.2188, 461.1660, 179.0347, and 161.0240. The ions at *m/z* 623.2188 and 461.1660 were separately corresponding to $[M-H-caffeoyl]^-$ and $[M-H-caffeoyl-Glc]^-$. The ion at *m/z* 179.0347 was corresponding to the loss of deprotonated caffeic acid as [caffeic acid-H]$^-$, and the ion at *m/z* 161.0240 was corresponding to [caffeic acid-H-H_2O]$^-$. Based on the accurate mass and compared with the standard, compound 43 was identified as echinacoside. Consistently, compounds 45 and 95 shared similar cleavage patterns with it and were identified as kankanoside F and 2′-acetylacteoside, respectively.

3.1.4. Phenylpropanoids

A total of 9 phenylpropanoids, consisting of simple phenylpropanoids, coumarins, and lignans, were analyzed in negative ion mode. Radix Rehmanniae Praeparata and Desertliving Cistanche were the primary sources of phenylpropanoids. These compounds primarily lose glycosyl groups and neutral molecules, with compound 16 serving as a brief example of their fragmentation pathways in mass spectrometry. Compound 16 showed the $[M-H]^-$ ion at *m/z* 341.0871, and its fragment ions at *m/z* 179.0347 and *m/z* 135.0449 were detected. The ion at *m/z* 179.0347 was generated by the loss of a glucosyl group, which was corresponding to $[M-H-Glc]^-$, and the ion at *m/z* 135.0449 was corresponding to the loss of a molecule carbon dioxide as $[M-H-Glc-CO_2]^-$. Based on the accurate mass and comparison with the cleavage pattern, compound 16 was identified as 6-O-caffeoylglucopyranose.

3.1.5. Organic acids

11 organic acids were discovered in positive and negative ion modes, which existed in the 7 herbs of THJGW. The structure of these compounds with a strong signal in negative ion mode contains carboxyl groups, which typically lose some neutral molecules. Considering compound 4 as an example, it gave a $[M-H]^-$ ion at *m/z* 191.0558, and the fragment ions at *m/z* 173.0448, 128.0434, 85.0287, 71.0133, and 59.0141. The ions at *m/z* 173.0448 and 128.0434 were separately corresponding to $[M-H-H_2O]^-$ and $[M-H-H_2O-HCOO]^-$, and the ions at *m/z* 85.0287, 71.0133, and 59.0141 were corresponding to the cleavage of cyclohexane. Based on the accurate mass and compared with the standard, compound 4 was identified as quinic acid.

3.1.6. Phenolics

4 phenolics were identified in both positive and negative ion modes, the majority of which came from Pyrola. The cleavage behaviors of these compounds in mass spectrometry were primarily due to the loss of substituents on the benzene ring. As an example, compound 115 showed a $[M + H]^+$ ion at *m/z* 153.0547, and the fragment ions at *m/z* 135.0438, 121.0284, and 93.0334, which were corresponding to $[M + H-H_2O]^+$, $[M + H-H_2O-CH_2]^+$, and $[M + H-H_2O-CH_2-CO]^+$, respectively. Based on the accurate mass and comparison with the cleavage pattern, compound 115 was identified as 3,4-dihydroxyacetophenone.

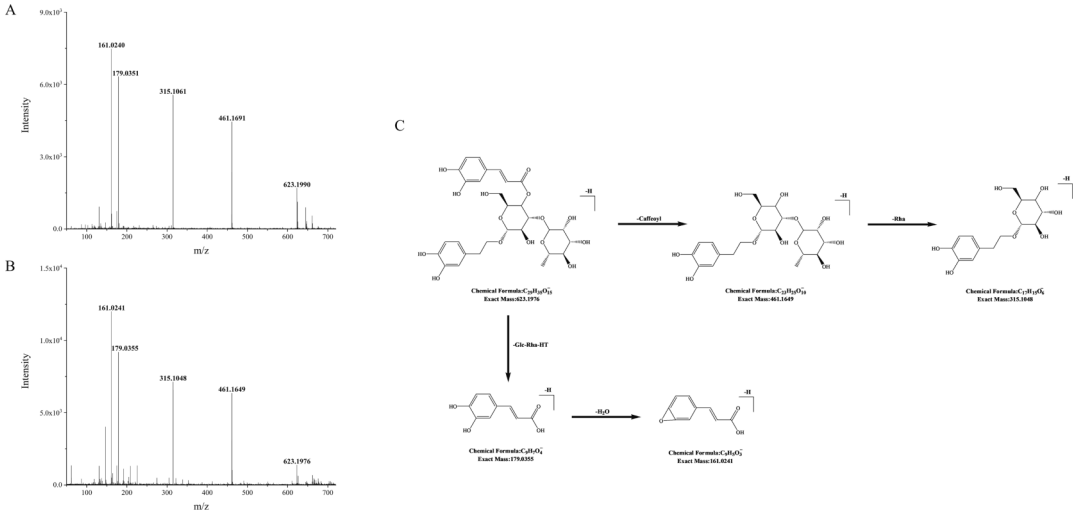

Fig. 4. MS/MS spectrum of acteoside standard **(A)** and acteoside **(B)**, as well as its possible cleavage pathway **(C)**.

3.1.7. Other compounds

Besides the above major compounds, 16 other compounds such as sugars, monoterpenoids, sterols, and glucosinoltes were identified from THJGW, and their mass spectrum information is shown in Table 1.

3.2. Target network pharmacology analysis

3.2.1. Analysis of absorbed components in serum

The pharmacokinetic parameters of major components among seven medicinal materials herbs in the formula were pre-searched and determined. Most of them had half-lives within 0.4–4 h and peak times within 0.16–2 h. Therefore, serum samples were collected in the 0–2 h range at 0.25, 0.5, 1, and 2 h points after the last dose in order to access more absorbed components efficiently. The serum samples from the blank group and various administration time groups were analyzed using the UPLC-Q-TOF-MS^{E} method, and their BPI chromatograms in positive and negative ion modes are shown in Fig. S3. A total of 38 prototype components were identified in serum samples using rapid matches with the UNIFI platform, as well as a comparison of retention times and fragment ions of each component from the chemical constituent analysis of THJGW. These components include 12 flavonoids, 8 organic acids, 6 iridoid glycosides, 2 phenolics, 2 phenylpropanoids, 1 phenylethanoid glycoside, and 7 other compounds. Most of them could be detected within 0.25 h after administration, while only 2 components remaining detectable at 2 h after administration. The mass spectrometry information for these compounds is detailed in Table S1.

3.2.2. Targets of active components and OA

3636 targets of 38 identified prototype absorbed components were predicted via the Swiss Target Prediction database platform, and 751 remained after removal of duplicates. A total of 3849 disease targets were acquired from the GeneCards database platform. Targets with a relevance score > 1 were screened and combined with the predicted targets from the OMIM and TTD database platforms. After removing duplicates, 1172 OA targets were obtained. Furthermore, 178 potential targets of THJGW for OA therapy were identified, and the venn diagram is shown in Fig. S4.

3.2.3. PPI network analysis

The PPI network of intersection targets was created with STRING and then imported into Cytoscape software for visualization, as shown in Fig. S5. The network consists of 142 nodes and 493 edges. The nodes represented targets, and the edges represented interactions between targets. Node size and color correspond to degree value, with smaller nodes and blue color indicating lower values and larger nodes and orange color indicating higher values. The degree value represents the importance of a node within the network, with a higher value indicating greater significance. The top 10 core targets ranked by MCC scores were VEGFA, STAT3, RELA/NF-κB p65, PIK3R1, PIK3CA, MMP9, MMP1, IL-6, HDAC1, and FGF2, respectively, as shown in Fig. S6.

3.2.4. Network topology analysis

Cytoscape was utilized to analyze and visualize the topology structure of the "herbs-components-targets-disease" network, as depicted in Fig. 5. The entire network includes 224 nodes and 1062 edges. The network topology was analyzed using CytoNCA and the top-ranked 11 key components were screened with high values of degree centrality (DC) and between centrality (BC), as shown in Table S2. Due to the large number of absorbed components, only these 11 components were selected and showed DC values ranging from 31.0 to 40.0.

3.2.5. GO enrichment and KEGG pathway analysis

GO function enrichment analysis was performed using Metascape, and the top 10 items were selected based on their p-value as shown in Fig. S7. The molecular functions (MF) category includes activities such as endopeptidase activity, protease binding, nuclear receptor activity, chemokine binding, and fibronectin binding. The biological processes (BP) category includes positive regulation of response to external stimulus, inflammatory response, response to hormone, response to molecule of bacterial origin, positive regulation of locomotion, and so on. The cellular components (CC) category includes the extracellular matrix, membrane raft, side of membrane, secretory granule lumen, lytic vacuole, and so on. KEGG pathway enrichment analysis resulted in Fig. S8, which displays the top 20 representative pathways as pathways in cancer, lipid and atherosclerosis, prostate cancer, microRNAs in cancer, transcriptional misregulation in cancer, and so on. This suggests that THJGW may have a role in the treatment of OA via these pathways. Further research focused on the lipid and atherosclerosis pathway due to its lower *p*-value and higher rich factor.

3.3. Molecular docking verification

It is widely assumed that binding energies less than −5.0 kcal/mol indicate favorable binding interactions between the compounds and targets. Lower the binding energy indicates stronger docking affinity. The molecular docking results among caffeic acid, acteoside, 8-prenylkaempferol, icaritin, rhein, naringenin, icariside II, baohuoside II, 5-(Glucosyl-α-1–6-glucose)-hydroxymethylfurfural (5-GGMF), 8-epiloganic acid, glucoraphenin and 10 core targets are shown in Fig. 6A. The binding energies of all docking results were in the range of −5.3 to −9.7 kcal/mol, indicating stable binding of these key components and core targets. This binding stability is closely correlated to the therapeutic effect of THJGW in treating OA disease. Notably, the core target proteins IL-6, STAT3, and RELA/NF-κB p65 had binding energies below

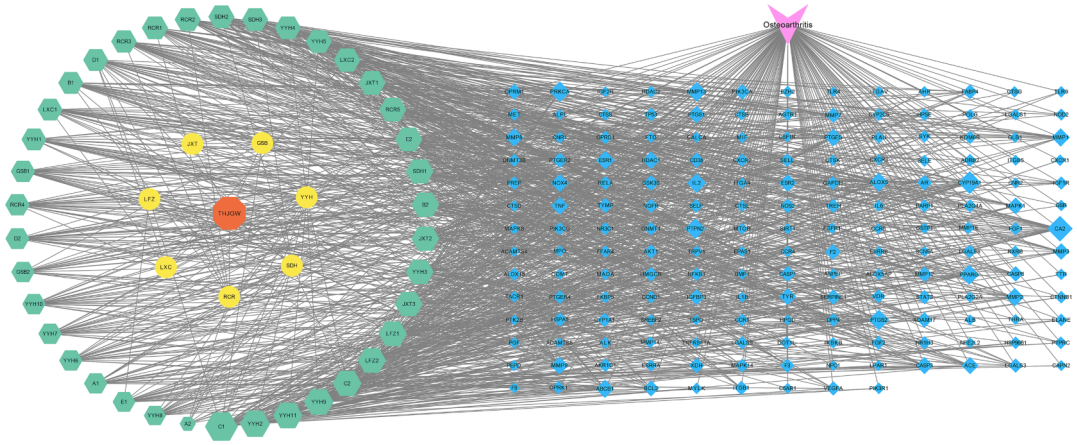

Fig. 5. "herbs-components-targets-disease" network of THJGW.

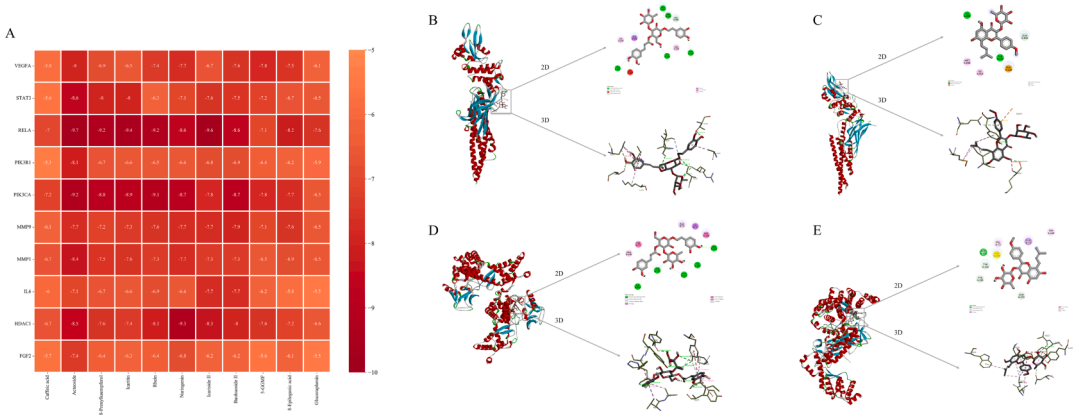

Fig. 6. Mollecular docking evaluation on the binding affinity of key components and core targets. **(A)** Heatmap of the molecular docking of 11 key components with 10 core targets. **(B)** Molecular docking model of STAT3 and acteoside; **(C)** Molecular docking model of STAT3 and icariside II; **(D)** Molecular docking model of RELA and acteoside; **(E)** Molecular docking model of RELA and icariside II.

−6.5 kcal/mol with strong binding affinity to most key components. It suggests that they are key targets of THJGW in the treatment of OA. Four of docking results with lower binding energies were visualized in Fig. 6B-E using the Discovery Studio software, and their complexes were primarily stabilized by hydrogen bonds and hydrophobic interactions.

3.4. Effects of THJGW on LPS-induced RAW264.7 macrophages

The MTT assay results, shown in Fig. S9, revealed that LPS at various concentrations reduced viability compared to untreated control cells. Among the tested concentrations, 1 μg/mL of LPS was chosen for the subsequent studies as it exhibited the lowest cell viability (Fig. S9A). THJGW exhibited no significant cytotoxicity at concentrations of 6.25–200 μg/mL in RAW264.7 cells, but significantly increased cell viability at a concentration of 50 μg/mL (Fig. S9B). Furthermore, THJGW had no significant cytotoxic effect on RAW264.7 cells stimulated by LPS (1 μg/mL), as shown in Fig. S9C. Pre-treatment with varying concentrations of THJGW had a distinct protective effects on cells compared to the LPS-induced group. However, this effect gradually attenuated with the increasing concentrations, particularly at 100 μg/mL, while cell viability was still higher than in the LPS-treated group. Consequently, concentrations of 6.25–50 μg/mL of THJGW were chosen for further experiments.

To investigate the anti-inflammatory effect of THJGW, LPS was used to stimulate RAW264.7 macrophages to imitate the chronic inflammatory environment. The ELISA results (Fig. 7A-B) showed a significant upregulation in the concentration of pro-inflammatory cytokines after LPS treatment for 24 h. The secretion of TNF-α and IL-6 in cell supernatants was visibly enhanced. However, pre-treatment with varying concentrations of THJGW prior to stimulation significantly diminished the increase of their secretion, and treatment with high concentrations (50 μg/mL) of THJGW notably suppressed the LPS-induced levels of TNF-α and IL-6.

3.5. THJGW inhibits the expression of phosphorylated STAT3 and NF-κB p65 in LPS-induced RAW264.7 cells

According to the results of target network pharmacology and molecular docking, STAT3 and NF-κB p65 were identified as key factors in the lipid and atherosclerosis pathway, playing a significant role in the treatment of THJGW on OA disease. Thus, to further investigate the effects of THJGW, we examined its impact on the expression levels of STAT3 and NF-κB p65 in LPS-stimulated RAW264.7 cells. According to the Western blot results in Fig. 8, STAT3 and NF-κB p65 proteins were

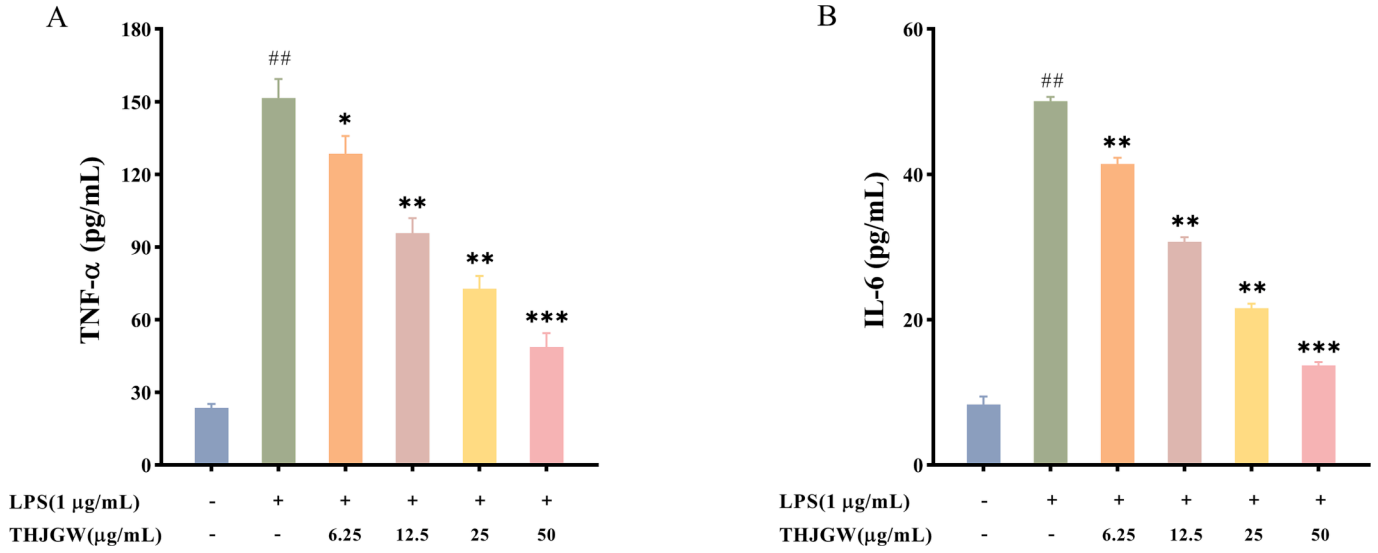

Fig. 7. Effects of THJGW on the secretion of TNF-α and IL-6 in LPS-induced RAW264.7 macrophages. **(A-B)** Concentrations of TNF-α and IL-6. All data are expressed as the mean ± SD. *vs.* control group ## $p < 0.01$. *vs.* LPS-treated group * $p < 0.05$, ** $p < 0.01$, *** $p < 0.001$.

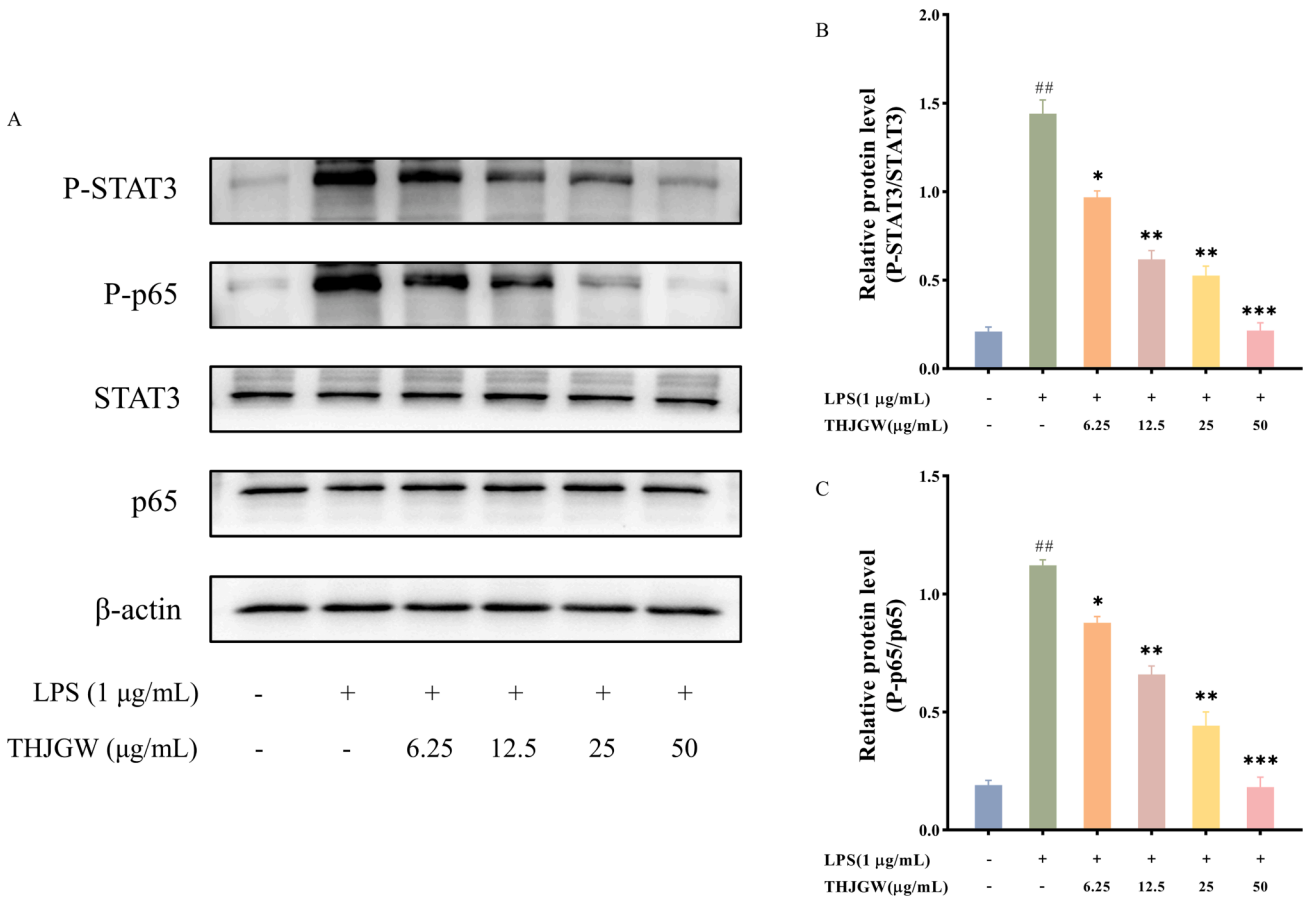

Fig. 8. Suppressive effects of THJGW on LPS-stimulated STAT3 and p65 phosphorylation in RAW264.7 macrophages. **(A)** Western blot protein bands; **(B-C)** Relative protein levels. The data are presented as means ± SD (n = 3). *vs.* control group ## $p < 0.01$. *vs.* LPS-treated group * $p < 0.05$, ** $p < 0.01$, *** $p < 0.001$.

slightly phosphorylated in the control group cells. However, inducing macrophages with LPS significantly increased the phosphorylation expression of these two proteins. The protein expression levels of P-STAT3 and P-p65 were significantly reduced with THJGW pretreatment, while it did not influence the expression of total STAT3 and NF-κB p65 proteins.

4. Discussion

In this study, a total of 134 components were identified from THJGW using the UPLC-Q-TOF-MS^E technology, and the possible cleavage pathways and chemical structures of its main compounds were determined. There were two major categories of compounds: 45 flavonoids and 39 phenylethanoid glycosides. The flavonoids mostly consist of 8-prenyl flavonoid O-glycosides, such as icariin and icariside II, which were typically loss glycosyl and neutral molecules in mass spectrometry. The phenylethanoid glycosides, such as echinacoside and acteoside, primarily cleave glycosyl, HT, and small molecules. Six major constituents in the THJG formula have been characterized by the UPLC method in a previous study (Li et al., 2021). Compared to the previous study, the in *vitro* chemical constituents of THJGW were characterized with greater accuracy, sensitivity, rapidity, and comprehensiveness using high-resolution mass spectrometry. This advanced characterization technique provided a solid foundation for subsequent research on the pharmacodynamic materials of THJGW in the current study.

Network pharmacology and molecular docking technology provided an effective tool for analyzing the active ingredients, targets, and pathways of TCM. In this study, target network pharmacology was utilized, which largely avoided the shortcomings of false positive target sites observed in traditional network pharmacology (Xu et al., 2017). A total of 38 prototype absorbed components from serum were identified using the UPLC-Q-TOF-MS^E method and were selected as candidates for the target network pharmacology analysis. The results showed that caffeic acid, 8-prenylkaempferol, icaritin, icariside II, acteoside, glucoraphenin, rhein, baohuoside II, naringenin, 8-epiloganic acid, and 5-GGMF were the key components of THJGW for treating OA. Previous studies suggested that caffeic acid may promote osteoblast proliferation, differentiation, and maturation, resulting in improved bone formation (Melguizo-Rodríguez et al., 2019). Icaritin, the metabolite of icariin, was found to have significant anti-inflammatory activity. It may reduce LPS-induced inflammatory responses in mouse chondrocytes by lowering nitric oxide and matrix metalloproteinases levels (Liu et al., 2010). Icariside II likely suppressed the progression of osteoporosis in rats by promoting osteoblast differentiation, inhibiting adipocyte formation, and modulating immune function (Xi et al., 2019). Acteoside was investigated to prevent bone loss in osteoporotic mice by inhibiting NF-κB and activating the PI3K/AKT signaling pathway (Yang et al., 2019). Naringenin has been proven in *vivo* and in *vitro* to be effective in treating iron overload-induced OA by alleviating cartilage damage and reducing oxidative stress levels (Pan et al., 2022). These reports mostly agreed with our predictions. However, there were also a few studies that held the opposite opinion. Folwarczna et al. discovered that caffeic acid did not minimize bone resorption in osteoporotic rats and may have altered bone mechanical properties in normal rats (Folwarczna et al., 2009), which could be attributed to oral administration. The PPI network analysis identified VEGFA, STAT3, RELA/NF-κB p65, PIK3R1, PIK3CA, MMP9, MMP1, IL-6, HDAC1, and FGF2 as key targets for THJGW in treating OA.

KEGG pathway analysis revealed that the top 10 core targets were significantly enriched in signaling pathways associated with anti-OA,

including pathways in cancer, lipid and atherosclerosis, prostate cancer, microRNAs in cancer, etc. Especially the lipid and atherosclerosis pathway, which was highly enriched by all ten core targets. Early observations revealed significant amounts of lipid deposition in osteoarthritic chondrocytes, implying a role for lipid metabolism in OA progression (Gkretsi et al., 2011). A majority of proteins related to lipid metabolism, such as peroxisome proliferator-activated receptor and apolipoproteins, were observed to be differentially expressed in osteoarthritic tissues based on several proteomic studies (Wu et al., 2007). Triantaphyllidou et al. have proposed that decreased content or disordered metabolism of high-density lipoprotein contributed to the OA development in metabolic syndrome mice, suggesting that this could be a key factor in OA pathogenesis (Triantaphyllidou et al., 2013). Moreover, studies have found that lipoproteins, which transport lipids in blood circulation, are the primary risk factor for atherosclerosis (Björkegren and Lusis, 2022). For instance, Han et al. have indicated that high-density lipoprotein produced by the intestine protects not only the liver but possibly also the vessel wall to avoid atherosclerosis (Han et al., 2021). However, certain triglyceride-rich lipoproteins directly contribute to the progression of atherosclerosis (Liu et al., 2017). Macêdo et al. have also discovered a link between atherosclerosis and OA pathogenesis (Macêdo et al., 2022). These studies support the predictions, indicating that the lipid and atherosclerosis pathway may be the primary approach for THJGW in the treatment of OA.

The molecular docking results suggested that 5 key components, including acteoside, icaritin, naringenin, icariside II, and baohuoside II, had higher binding affinities to most of the core targets. Additionally, three core targets, which were IL-6, STAT3, and RELA/NF-κB p65, had higher binding energies for most key components. Previous studies have shown that IL-6 has multiple catabolic functions in cartilage, which were primarily mediated by STAT3, and the IL-6 pathway may be useful as a targeted therapy for OA to alleviate cartilage damage, synovial inflammation, and subchondral bone pathology (Latourte et al., 2016). In *vivo* and in *vitro* experiments have shown that the STAT3 pathway may regulate cartilage degradation, with activation leading to cartilage damage and osteophyte formation in OA (Latourte et al., 2017). Kobayashi et al. have proven that NF-κB family member p65 may inhibit chondrocyte apoptosis and participate in the regulation of articular cartilage homeostasis in OA, but canonical activation of the NF-κB signaling pathway promotes cartilage catabolism (Kobayashi et al., 2016). Molecular docking results support the accuracy of target network pharmacology predictions.

The therapeutic effects of herbs in the formula have been reported in several studies. Jhun et al. found that an extract of Radix Rehmanniae Praeparata alleviated inflammatory symptoms and articular cartilage degradation in monosodium iodoacetate-induced OA rats by inhibiting NF-κB and HIF-2α activation (Jhun et al., 2018). Dai et al. discovered that the combination of Rhizoma Drynariae and Epimedium brevicornum inhibited the phosphorylation expression of p38, ERK, and JNK proteins in rat cartilage tissue, thereby preventing OA development via the MAPK signaling pathway (Dai, 2022). Spatholobus extract was observed to prevent bone loss through the inhibition of osteoclast differentiation, indicating that it may have therapeutic potential to attenuate cartilage damage in OA (Im et al., 2014). Likewise, Zhang et al. have demonstrated that Desertliving Cistanche may suppress osteoclast differentiation and corresponding bone resorption in an osteoporosis rat model (Zhang et al., 2019). However, the molecular mechanisms of THJGW in OA treatment need to be determined and thoroughly investigated. Recent clinical studies have provided substantial evidence that inflammation is key driver of OA disease (Knights et al., 2023). Excessive levels of inflammatory mediators such as IL-6, IL-1β, and TNF have been detected in chondrocytes and synovial cells in OA, thus targeting inflammatory therapy might be an effective treatment to prevent or slow OA progression (Robinson et al., 2016). Previous studies have suggested that macrophages contributed substantially to the progression of OA through various secreted mediators that may regulate joint inflammation (Wu et al., 2020a). Therefore, RAW264.7 macrophages were used to mimic an inflammatory environment in *vitro* to verify the mechanism of THJGW in treating OA. Inflammatory cytokine levels in cell supernatants were substantially increased by LPS (1 μg/mL)-treated RAW264.7 cells, which was significantly reversed by pre-treatment of THJGW at a high concentration (50 μg/mL). The results indicated that the anti-inflammatory effect of THJGW was attributed to inhibiting the pro-inflammatory cytokines, namely TNF-α and IL-6, in LPS-induced RAW264.7 cells. Furthermore, molecular docking results identified STAT3 and RELA/NF-κB p65 as key targets associated with the lipid and atherosclerosis pathway. Wu et al. have demonstrated that inhibition of the phosphorylated expression of these two proteins in macrophages is beneficial for the treatment of inflammatory diseases (Wu et al., 2020b). Our results indicated that expression of phosphorylated STAT3 and NF-κB p65 proteins was visibly increased in LPS-induced cells, suggesting activation of the lipid and atherosclerosis pathway. THJGW pre-treatment significantly restored the phosphorylation levels of STAT3 and NF-κB p65 proteins without affecting total proteins. These findings implied that THJGW effectively inhibits the phosphorylation of STAT3 and NF-κB p65 proteins in LPS-induced macrophages, thereby mediating the lipid and atherosclerosis pathway to exert an anti-inflammatory effect in OA.

5. Conclusion

In the current study, the pharmacodynamic material and mechanism of action of THJGW in OA treatment were investigated. A total of 134 chemical constituents of THJGW in *vitro* were analyzed by UPLC-Q-TOF-MS technology, and the majority of them were flavonoids and phenylethanoid glycosides. Similarly, 38 prototype absorbed components were identified in serum and considered candidates. The key components acteoside, icaritin, naringenin, icariside II, and baohuoside II, as well as the core targets IL-6, STAT3, and RELA/NF-κB p65, which were closely associated with therapeutic effects on OA for THJGW, were predicted and validated by targeted network pharmacology and molecular docking technique. Moreover, LPS-induced RAW264.7 macrophages were used in in *vitro* assays for inflammation. The outcomes further confirmed and indicated that THJGW, possibly through inhibition of the lipid and atherosclerosis pathway, has a potent anti-inflammatory effect in OA. This suppression was achieved through a reduction in the expression levels of inflammatory cytokines TNF-α and IL-6, as well as phosphorylation of STAT3 and NF-κB p65 proteins. In conclusion, this research strategy offers a fresh perspective on how to examine the pharmacodynamic material basis and its mechanism in Chinese medicine. The research findings provide scientific evidence for the scientific application and improvement of quality standards for THJGW. However, this study also has certain limitations. The screened active compounds were not further validated and deeply investigated in terms of their activities and mechanisms of action, and part of this work will be continued in our subsequent studies.

CRediT authorship contribution statement

Dong Xie: Formal analysis, Investigation, Visualization, Writing – original draft. **Guangfu Lv:** Methodology. **Yuchen Wang:** Methodology. **Wenjing Zhang:** Software. **Nian Li:** Software. **Yao Duan:** Software. **Qing Huang:** Resources. **Ge Chen:** Conceptualization, Writing – review & editing. **Zifeng Pi:** Conceptualization, Writing – review & editing. **Hao Yue:** Conceptualization, Writing – review & editing.

Declaration of Competing Interest

The authors declare that they have no known competing financial interests or personal relationships that could have appeared to influence the work reported in this paper.

Acknowledgements

This research was supported by Science and Technology Development Project of Jilin Province (20210401064YY and 20210508001RQ).

Appendix A. Supplementary data

Supplementary data to this article can be found online at https://doi.org/10.1016/j.arabjc.2024.105711.

References

Björkegren, J.L.M., Lusis, A.J., 2022. Atherosclerosis: recent developments. Cell 185, 1630–1645. https://doi.org/10.1016/j.cell.2022.04.004.

Chang, H., Lv, S., Yuan, T., Wu, H., Wang, L., Sang, R., Zhang, C., Chen, W., 2021. Identification and Analysis of Chemical Constituents and Rat Serum Metabolites in Gushuling Using UPLC-Q-TOF/MS Coupled with Novel Informatics UNIFI Platform. Evid-Based. Compl. Alt. 2021, 2894306. https://doi.org/10.1155/2021/2894306.

Chen, Y., Xue, Y., Wang, X., Jiang, D., Xu, Q., Wang, L., Zheng, Y., Shi, Y., Cao, Y., 2023. Molecular Mechanism of the Guizhi Decoction on Osteoarthritis based on an Integrated Network Pharmacology and RNA-sequencing Approach with Experimental Validation. Front. Genet. 14, 1079631. https://doi.org/10.3389/fgene.2023.1079631.

Cheng, F., Desai, R.J., Handy, D.E., Wang, R., Schneeweiss, S., Barabási, A.L., Loscalzo, J., 2018. Network-based approach to prediction and population-based validation of in silico drug repurposing. Nat. Commun. 9, 2691. https://doi.org/10.1038/s41467-018-05116-5.

Dai, Z., 2022. Study on the Protective effect and mechanism of the rhizoma drynariae-Epimedium Formula on osteoarthritis in rats. Contrast. Media. Mol. i. 2022, 2869707. https://doi.org/10.1155/2022/2869707.

Folwarczna, J., Zych, M., Burczyk, J., Trzeciak, H., Trzeciak, H.I., 2009. Effects of natural phenolic acids on the skeletal system of ovariectomized rats. Planta Med. 75, 1567–1572. https://doi.org/10.1055/s-0029-1185904.

Gkretsi, V., Simopoulou, T., Tsezou, A., 2011. Lipid metabolism and osteoarthritis: lessons from atherosclerosis. Prog. Lipid. Res. 50, 133–140. https://doi.org/10.1016/j.plipres.2010.11.001.

Han, Y.H., Onufer, E.J., Huang, L.H., Sprung, R.W., Davidson, W.S., Czepielewski, R.S., Wohltmann, M., Sorci-Thomas, M.G., Warner, B.W., Randolph, G.J., 2021. Enterically derived high-density lipoprotein restrains liver injury through the portal vein. Science 373, eabe6729. https://doi.org/10.1126/science.abe6729.

Im, N.K., Lee, S.G., Lee, D.S., Park, P.H., Lee, I.S., Jeong, G.S., 2014. Spatholobus suberectus inhibits osteoclastogenesis and stimulates chondrogenesis. Am. J. Chin. Med. 42, 1123–1138. https://doi.org/10.1142/S0192415X14500700.

Jhun, J.Y., Na, H.S., Shin, J.W., Jung, K.A., Seo, H.B., Ryu, J.Y., Choi, J.W., Moon, S.J., Park, H.J., Oh, S.W., et al., 2018. Notoginseng radix and rehmanniae radix preparata extract combination (YH23537) reduces pain and cartilage degeneration in rats with monosodium iodoacetate-induced osteoarthritis. J. Med. Food 21, 745–754. https://doi.org/10.1089/jmf.2017.4041.

Kang, L.P., Yu, K., Zhao, Y., Liu, Y.X., Yu, H.S., Pang, X., Xiong, C.Q., Tan, D.W., Gao, Y., Liu, C., Ma, B.P., 2012. Characterization of steroidal glycosides from the extract of Paris Polyphylla var. Yunnanensis by UPLC/Q-TOF MSE. J. Pharm. Biomed. Anal. 62, 235–249. https://doi.org/10.1016/j.jpba.2011.12.027.

Knights, A.J., Redding, S.J., Maerz, T., 2023. Inflammation in osteoarthritis: the latest progress and ongoing challenges. Curr. Opin. Rheumatol. 35, 128–134. https://doi.org/10.1097/BOR.0000000000000923.

Kobayashi, H., Chang, S.H., Mori, D., Itoh, S., Hirata, M., Hosaka, Y., Taniguchi, Y., Okada, K., Mori, Y., Yano, F., et al., 2016. Biphasic regulation of chondrocytes by Rela through induction of anti-apoptotic and catabolic target genes. Nat. Commun. 7, 13336. https://doi.org/10.1038/ncomms13336.

Kraus, V.B., Blanco, F.J., Englund, M., Karsdal, M.A., Lohmander, L.S., 2015. Call for standardized definitions of osteoarthritis and risk stratification for clinical trials and clinical use. Osteoarthritis and Cartilage 23, 1233–1241. https://doi.org/10.1016/j.joca.2015.03.036.

Latourte, A., Maillet, J., Cherifi, C., Ea, H., Bouaziz, W., Funck-Brentano, T., Cohen-Solal, M., Hay, E., Richette, P., 2016. IL-6/STAT3 signalling blockade protects against experimental osteoarthritis in mice. Osteoarthritis and Cartilage 24, S378. https://doi.org/10.1016/j.joca.2016.01.674.

Latourte, A., Cherifi, C., Maillet, J., Ea, H.K., Bouaziz, W., Funck-Brentano, T., Cohen-Solal, M., Hay, E., Richette, P., 2017. Systemic inhibition of IL-6/Stat3 signalling protects against experimental osteoarthritis. Ann. Rheum. Dis. 76, 748–755. https://doi.org/10.1136/annrheumdis-2016-209757.

Li, S., Sun, Y., Lu, L., Yang, C., Zhou, Z., Cui, L., Lu, B., Yin, F., Zhang, Y., 2021. In vivo effect of the Chinese Tenghuang Jiangu Formula on cartilage destruction and subchondral bone sclerosis. Phytomedicine plus 1, 100121. https://doi.org/10.1016/j.phyplu.2021.100121.

Lin, P., Hu, L.F., Huang, Q.T., Zhang, Y.Z., Qin, Z.F., Chen, J.X., Yao, X.S., Wu, H.L., Yao, Z.H., Xu, D.P., 2023. Pharmacokinetics integrated with network pharmacology to clarify effective components and mechanism of Wendan decoction for the intervention of coronary heart disease. J. Ethnopharmacol. 314, 116669. https://doi.org/10.1016/j.jep.2023.116669.

Liu, W., Chen, X.H., Ge, Y.Y., Wang, H.L., Phosat, C., Li, J., Mao, H.P., Gao, X.M., Chang, Y.X., 2020. Network pharmacology strategy for revealing the pharmacological mechanism of pharmacokinetic target components of San-Ye-Tang-Zhi-Qing formula for the treatment of type 2 diabetes mellitus. J. Ethnopharmacol. 260, 113044. https://doi.org/10.1016/j.jep.2020.113044.

Liu, D.J., Peloso, G.M., Yu, H., Butterworth, A.S., Wang, X., Mahajan, A., Saleheen, D., Emdin, C., Alam, D., Alves, A.C., et al., 2017. Exome-wide association study of plasma lipids in> 300,000 individuals. Nat. Genet. 49, 1758–1766. https://doi.org/10.1038/ng.3977.

Liu, M.H., Sun, J.S., Tsai, S.W., Sheu, S.Y., Chen, M.H., 2010. Icariin protects murine chondrocytes from lipopolysaccharide-induced inflammatory responses and extracellular matrix degradation. Nutr. Res. 30, 57–65. https://doi.org/10.1016/j.nutres.2009.10.020.

Liu, C.S., Xia, T., Luo, Z.Y., Wu, Y.Y., Hu, Y.N., Chen, F.L., Tang, Q.F., Tan, X.M., 2021. Network pharmacology and pharmacokinetics integrated strategy to investigate the pharmacological mechanism of Xianglian pill on ulcerative colitis. Phytomedicine 82, 153458. https://doi.org/10.1016/j.phymed.2020.153458.

Macêdo, M.B., Santos, V.M.O.S., Pereira, R.M.R., Fuller, R., 2022. Association between osteoarthritis and atherosclerosis: A systematic review and meta-analysis. Exp. Gerontol. 161, 111734. https://doi.org/10.1016/j.exger.2022.111734.

Melguizo-Rodríguez, L., Manzano-Moreno, F.J., Illescas-Montes, R., Ramos-Torrecillas, J., de Luna-Bertos, E., Ruiz, C., García-Martínez, O., 2019. Bone protective effect of extra-virgin olive oil phenolic compounds by modulating osteoblast gene expression. Nutrients 11, 1722. https://doi.org/10.3390/nu11081722.

Pan, Z., He, Q., Zeng, J., Li, S., Li, M., Chen, B., Yang, J., Xiao, J., Zeng, C., Luo, H., Wang, H., 2022. Naringenin protects against iron overload-induced osteoarthritis by suppressing oxidative stress. Phytomedicine 105, 154330. https://doi.org/10.1016/j.phymed.2022.154330.

Robinson, W.H., Lepus, C.M., Wang, Q., Raghu, H., Mao, R., Lindstrom, T.M., Sokolove, J., 2016. Low-grade inflammation as a key mediator of the pathogenesis of osteoarthritis. Nat. Rev. Rheumatol. 12, 580–592. https://doi.org/10.1038/nrrheum.2016.136.

Sharma, L., 2021. Osteoarthritis of the knee. N. Engl. J. Med. 384, 51–59. https://doi.org/10.1056/NEJMcp1903768.

Triantaphyllidou, I.E., Kalyvioti, E., Karavia, E., Lilis, I., Kypreos, K.E., Papachristou, D. J., 2013. Perturbations in the HDL metabolic pathway predispose to the development of osteoarthritis in mice following long-term exposure to western-type diet. Osteoarthritis and Cartilage 21, 322–330. https://doi.org/10.1016/j.joca.2012.11.003.

Wang, Y., Zhang, Y., Wang, Y., Shu, X., Lu, C., Shao, S., Liu, X., Yang, C., Luo, J., Du, Q., 2021. Using network pharmacology and molecular docking to explore the mechanism of Shan Ci Gu (Cremastra appendiculata) against non-small cell lung cancer. Front. Chem. 9, 682862. https://doi.org/10.3389/fchem.2021.682862.

Wu, J.Y., Chen, Y.J., Bai, L., Liu, Y.X., Fu, X.Q., Zhu, P.L., Li, J.K., Chou, J.Y., Yin, C.L., Wang, Y.P., et al., 2020b. Chrysoeriol ameliorates TPA-induced acute skin inflammation in mice and inhibits NF-κB and STAT3 pathways. Phytomedicine 68, 153173. https://doi.org/10.1016/j.phymed.2020.153173.

Wu, C.L., Harasymowicz, N.S., Klimak, M.A., Collins, K.H., Guilak, F., 2020a. The role of macrophages in osteoarthritis and cartilage repair. Osteoarthritis and Cartilage 28, 544–554. https://doi.org/10.1016/j.joca.2019.12.007.

Wu, J., Liu, W., Bemis, A., Wang, E., Qiu, Y., Morris, E.A., Flannery, C.R., Yang, Z., 2007. Comparative proteomic characterization of articular cartilage tissue from normal donors and patients with osteoarthritis. Arthritis. Rheum. 56, 3675–3684. https://doi.org/10.1002/art.22876.

Xi, Y., Jiang, T., Yu, J., Xue, M., Xu, N., Wen, J., Wang, W., He, H., Ye, X., 2019. Preliminary studies on the anti-osteoporosis activity of Baohuoside I. Biomed. Pharmacother. 115, 108850. https://doi.org/10.1016/j.biopha.2019.108850.

Xu, T., Li, S., Sun, Y., Pi, Z., Liu, S., Song, F., Liu, Z., 2017. Systematically characterize the absorbed effective substances of Wutou Decoction and their metabolic pathways in rat plasma using UHPLC-Q-TOF-MS combined with a target network pharmacological analysis. J. Pharm. Biomed. Anal. 141, 95–107. https://doi.org/10.1016/j.jpba.2017.04.012.

Yan, C., An, F., Jiang, G., Zhao, C., Li, J., Li, M., Guo, D., 2020. Effect of Tenghuangjiangu capsule on the expression of blood cell and inflammatory cytokines in rats with knee osteoarthritis. J. Biol. 37, 84–87. https://doi.org/10.3969/j.issn.2095-1736.2020.06.084.

Yang, L., Zhang, B., Liu, J., Dong, Y., Li, Y., Li, N., Zhao, X., Snooks, H., Hu, C., Ma, X., 2019. Protective effect of acteoside on ovariectomy-induced bone loss in mice. Int. J. Mol. Sci. 20, 2974. https://doi.org/10.3390/ijms20122974.

Zhang, B., Yang, L.L., Ding, S.Q., Liu, J.J., Dong, Y.H., Li, Y.T., Li, N., Zhao, X.J., Hu, C.L., Jiang, Y., Ma, X.Q., 2019. Anti-osteoporotic activity of an edible traditional Chinese medicine Cistanche deserticola on bone metabolism of ovariectomized rats through RANKL/RANK/TRAF6-mediated signaling pathways. Front. Pharmacol. 10, 1412. https://doi.org/10.3389/fphar.2019.01412.

Zhao, H., Wang, Y., Xu, C., Li, G.J., Song, Y.W., Qiu, J.J., Cui, L.M., Song, X.C., Yang, Y. J., Sun, Y., 2023. Potential molecular mechanisms of Erlongjiaonang action in idiopathic sudden hearing loss: A network pharmacology and molecular docking analyses. Front. Neurol. 14, 1121738. https://doi.org/10.3389/fneur.2023.1121738.